Bulletin of Mathematical Biology manuscript No.
(will be inserted by the editor)

Venu Kurella · Justin C. Tzou · Daniel Coombs · Michael J. Ward

Asymptotic Analysis of First Passage Time Problems Inspired by Ecology

Received: date / Revised: date

Abstract A hybrid asymptotic-numerical method is formulated and implemented to accurately calculate the mean first passage time (MFPT) for the expected time needed for a predator to locate small patches of prey in a 2-D landscape. In our analysis the movement of the predator can have both a random and a directed component, where the diffusivity of the predator is isotropic but possibly spatially heterogeneous. Our singular perturbation methodology, which is based on the assumption that the ratio ε of the radius of a typical prey patch to that of the overall landscape is asymptotically small, leads to the derivation of an algebraic system that determines the MFPT in terms of parameters characterizing the shapes of the small prey patches together with a certain Green's function, which in general must be computed numerically. The expected error in approximating the MFPT by our semi-analytical procedure is smaller than any power of $-1/\log\varepsilon$, so that our approximation of the MFPT is still rather accurate at only moderately small prey patch radii. Overall, our hybrid approach has the advantage of eliminating the difficulty with resolving small spatial scales in a full numerical treatment of the partial differential equation (PDE). Similar semi-analytical methods are also developed and implemented to accurately calculate related quantities such as the variance of the mean first passage time (VMFPT) and the splitting probability. Results for the MFPT, the VMFPT, and splitting probability obtained from our hybrid methodology are validated with corresponding results computed from full numerical simulations of the underlying PDE's.

Keywords Mean first passage time · centralizing tendency · Neumann Green's function · matched asymptotic expansions · splitting probability

Mathematics Subject Classification (2000) 35B25 · 35J25 · 92D40

1 Introduction

Geography and movement are very important factors in determining the population dynamics of predator-prey systems in ecology [28, 34, 53]. For example, the distribution of predator dens across the landscape affects prey survival, while

Venu Kurella
School of Computational Science and Engineering, McMaster University, Hamilton, Ontario, Canada
E-mail: kurellv@mcmaster.ca

Justin C. Tzou
Dept. of Mathematics and Statistics, Dalhousie Univ., Halifax, Nova Scotia, Canada
E-mail: tzou.justin@gmail.com

Daniel Coombs
Institute of Applied Mathematics and Dept. of Mathematics, Univ. of British Columbia, Vancouver, B.C., Canada
E-mail: coombs@math.ubc.ca

Michael J. Ward (corresponding author)
Institute of Applied Mathematics and Dept. of Mathematics, Univ. of British Columbia, Vancouver, B.C., Canada
E-mail: ward@math.ubc.ca

localized prey foraging sites can impact the success of predators. Similarly, predators hunting for prey experience physical limitations on movement imposed by the landscape (for example, thick brush versus open forest), that may lead to restrictions on their rate of finding food. As a specific example, the distribution of wolves in forested regions is known to be influenced by topography, competing species, and the density of prey [36, 37]. Additionally, human alterations to the landscape (and in particular the introduction of linear features such as roads and seismic surveying lines) have all been implicated in altering the motion of both wolves and their prey species (caribou and elk) across the landscape [17, 26, 27, 36, 57, 58]. Since time elapsed and distance covered before successful hunting are factors that determine the fitness and survival of a predator, it is important to understand how the locations and movement of both predator and prey can affect reproductive fitness and probability of survival. This is particularly important when considering the potential effects of human effects of human alterations to the landscape, such as vegetation changes, road-building, power line cuts, etc.

In this paper, we will present hybrid numerical-analytical results for the first passage time approach to estimating predator search times under the assumption that predator movement is well described by random walk models (Brownian motion). The mean first passage time (MFPT) approach was first used in an ecological context by McKenzie et. al. [35], but their work was based on pre-existing theory for physical and chemical systems (see e.g. [12, 18, 41] etc). In the ecological context, the MFPT, T, is the mean time taken for a predator to reach a specific patch (with prey) for the first time, starting from a given location in some two-dimensional spatial landscape. Since this time may vary depending on the start location, we define $T(\mathbf{X})$ as the mean time taken for the predator to reach its target for the first time, starting from the location $\mathbf{X}$. The target could for instance be a prey patch, representing a spatial region around the prey, within which the predator can locate and attack the prey. The approximation of a static prey patch is justified if we consider a predator seeking a relatively stationary prey that has a very small home range. Here, we suppose that the predator will always catch the prey if it enters the prey patch (this is a 'hard encounter' in the language of Gurarie and Ovaskainen [20]). For analytical tractability, we will only consider the case where the prey patches are stationary in time.

The fundamental assumption underlying many first passage time models is that animal motion can be reasonably well described by a spatial diffusion process. This assumption can be justified on the macroscopic scale via the central limit theorem, and has been in common use in ecological modelling for a long time [4, 20, 35–38, 46, 54]. Different diffusion-like models can be considered. The simplest possible model is pure diffusion, equivalent to molecular Brownian motion with a diffusivity D. Alternatively, drift-diffusion models incorporate an underlying directed motion, or drift, and in particular this can be used to build a "home-range" model of animal movement, where a centralizing directed motion is imposed towards a fixed den-site for the predator, in addition to a purely diffusive motion [22, 38]. Alternatively, spatial variability in animal motion can be captured through a spatially-variable diffusion coefficient [11, 36]. Generically, all these models based on diffusion processes lead us to a two-dimensional backward Kolmogorov equation, an elliptic partial differential equation (PDE) for the MFPT with prescribed boundary conditions at prey patches and habitat boundaries [35, 41]. This equation can be solved analytically for simple spatial domains, but in many studies, numerical methods have been applied to approximate the solution [2, 19, 24, 25, 36].

However, in many other contexts it has proven possible to establish the MFPT as an asymptotic series, using singular perturbation theory (e.g. [13, 15, 39], etc. for microscopic cell-scale and physiological studies that use this approach.) The key requirement is that the target region is a small, localized structure compared to the overall region where the motion occurs. In the present context, this is the assumed small ratio of a prey patch size to the whole predator habitat. In this small ratio limit, we will use singular perturbation techniques to analytically derive an algebraic system that determines the MFPT in terms of a certain Green's function, which in general must be computed numerically. This overall hybrid asymptotic-numerical approach has the benefit of eliminating the difficulty with resolving small spatial scales in a full numerical treatment of the PDE. Our semi-analytical approach also gives considerable insight into the dependence of the MFPT on the system parameters.

Two further concepts related to the MFPT for a diffusing particle in the presence of trap(s) are the *variance of the MFPT* (VMFPT) and the *splitting probability*. For situations where the first passage time has a significant spread about the mean, it may be important to estimate the second moment (SMFPT) of the first passage time. We show how to extend our hybrid asymptotic-numerical method for the MFPT to asymptotically calculate the SMFPT in the presence of small patches. By using $\text{VMFPT} = \text{SMFPT} - \text{MFPT}^2$, we are then able to determine the VMFPT. The second concept related to the MFPT is that of the splitting probability. The splitting probability is defined as the probability that a dynamic particle reaches one particular target patch before reaching any of the other patches, an is well-known to satisfy Laplace's equation in a domain with small traps (cf. [41, 45]). In the context of ecology, the splitting probability arises in calculating the probability of a predator reaching a specific prey patch in a landscape consisting of other prey patches. Similar calculations in two-dimensional domains with small circular patch targets, but with applications to biophysical modeling, have been performed in [9] using a pseudo-potential method. However, we show that our hybrid asymptotic-numerical technique can yield a very high level of accuracy, and can be used for both arbitrarily-shaped prey patches and for the case where the target patch is very close to a neighboring patch. The analysis and applications related to both the

VMFPT and the splitting probability are novel, and results from our asymptotic theory are found to agree very closely with corresponding results computed from full PDE simulations.

The problems under consideration herein can be referred to as *n*arrow capture problems, where the time needed for a Brownian particle to reach a small compact target in a 2-D domain is asymptotically long as the radius of the target tends to zero. Related biophysical problems involving either searching for small binding sites in a biological cell or diffusive processes undergoing localized chemical reactions in small localized regions are formulated and studied in [3], [5], [6], [9], [12], [23], [47], and [49]. A related class of problems, known as *narrow escape problems*, where a Brownian particle can exit a domain only through a small window on its boundary, have been studied in [43], [42], [39], [8], and [7]. For a broad survey of such problems and their applications to biophysical modeling see [21] and [44] and the references therein. From a mathematical viewpoint, narrow capture and escape problems are singular perturbation problems where the perturbation is strong but localized in space. Strong localized perturbation theory, which initiates partially from [55] and [56], has been developed and applied over the past two decades to treat various PDE and eigenvalue problems in 2-D or 3-D domains containing small defects (cf. [10], [13], [30], [52]).

Diffusive processes in the presence of a centralizing drift term also arise in the biophysical modeling of the trafficking of viral particles in the cell cytoplasm (cf. [1, 31–33, 50]). In this 3-D context, the viral particles first cross the cell membrane and then undergo Brownian motion with intermittent drift along microtubules that direct the particles towards the target site, being the cell nucleus. The analysis of first passage time quantities associated with this class of problems is given in [31–33]. In our 2-D ecological context, we also assume a centralizing drift term, but in contrast to the problems considered in [31–33], we assume there are N possible small target sites in an arbitrary 2-D domain.

The outline of this paper is as follows. In §2 we develop a hybrid asymptotic-numerical method to asymptotically calculate the MFPT in a 2-D landscape of small patches when the assumed isotropic diffusivity is spatially homogeneous. For this problem, we allow for a possible drift term that models a centralizing tendency of the predator. In §3.1 results from the asymptotic theory for the MFPT are compared with full numerical simulations of the corresponding PDE for a circular landscape. In our comparisons we use the parameter values of [35] for the constant diffusivity, the magnitude of the drift velocity, and typical sizes of both the landscape and a prey patch. In §4 we extend our semi-analytical theoretical framework to calculate the MFPT for the case of an isotropic, but spatially variable diffusivity. In §5 we show how to asymptotically calculate the splitting probability in a landscape of small patches, while in §6 we asymptotically solve the PDE characterizing the SMFPT. The asymptotic results in §4–6 are illustrated for various prey patch configurations, and are favorably compared with results obtained from full numerical simulations of the corresponding PDE's. Finally, in §7 we give a brief discussion of some open problems.

2 The Mean First Passage Time

It is well-known that the MFPT, $T(\mathbf{X})$, satisfies the following elliptic PDE in a two-dimensional domain (cf. [41]):

$$D\Delta' T(\mathbf{X}) + \mathbf{c}(\mathbf{X}) \cdot \nabla' T(\mathbf{X}) = -1\,, \tag{2.1}$$

where D is the diffusivity of the underlying Brownian motion, and $\mathbf{c}(\mathbf{X})$ is the drift velocity. As similar to the modeling of the trafficking of viral particles in the cell cytoplasm (cf. [31, 50]), (2.1) can be derived from the homogenization limit of a diffusive process whereby the predator undergoes both free diffusion and intermittent directed motion.

In (2.1), we assume that the drift velocity $\mathbf{c}$ is a conservative vector field, and so can be written as the gradient of some scalar potential. With this assumption, the divergence structure of (2.1) is preserved, and the analysis of (2.1) is considerably more tractable than for the case of arbitrary drift. For our problem, where the predator has a centralizing tendency, the drift $\mathbf{c}$ is a conservative field directed towards the origin (see §3.1 below for our choice of $\mathbf{c}$).

The system (2.1) is made dimensionless by introducing the new variables u, $\mathbf{x}$, and $\psi(\mathbf{x})$ as $u = \frac{D}{L^2}T$, $\mathbf{x} = L^{-1}\mathbf{X}$ and $\nabla\psi = c(\mathbf{X})\frac{L}{D}$. The primed derivatives are defined with respect to $\mathbf{X}$ while the un-primed ones are defined with respect to the non-dimensional variable $\mathbf{x}$. Here $2L$ is the characteristic diameter of the domain under consideration. In particular, for a circular landscape, L is the radius of the landscape. The non-dimensional PDE problem for the MFPT, assuming the presence of N localized prey patches, is formulated as

$$\begin{aligned} \Delta u(\mathbf{x}) + \nabla\psi(\mathbf{x}) \cdot \nabla u(\mathbf{x}) = -1\,, \quad \mathbf{x} \in \Omega \setminus \cup_{j=1}^{N} \Omega_j^\varepsilon\,; \qquad \frac{\partial u}{\partial n} = 0\,, \quad \mathbf{x} \in \partial\Omega\,, \\ u = 0\,, \qquad \mathbf{x} \in \partial\Omega_j^\varepsilon\,, \quad j = 1\ldots, N\,. \end{aligned} \tag{2.2}$$

The non-dimensional MFPT satisfies the PDE (2.2) in the landscape Ω, which is perforated by N prey patches of small area denoted by $\Omega_1^\varepsilon, \ldots, \Omega_N^\varepsilon$ (see Fig. 1). The MFPT vanishes on the boundary of each patch, and satisfies a reflecting boundary condition on the domain boundary. We assume that the domain Ω has diameter $\mathcal{O}(1)$ while the non-dimensional

radius of each patch is $\mathcal{O}(\varepsilon)$, where $\varepsilon \ll 1$. As $\varepsilon \to 0$, we assume that $\Omega_j^\varepsilon \to \mathbf{x}_j$, so that each patch shrinks to a point in Ω as $\varepsilon \to 0$. We also assume that the distance between any two patches is $\mathcal{O}(1)$ as $\varepsilon \to 0$. In our analysis below the landscape Ω is an arbitrary bounded domain. However, as was done in [35], in §3 we illustrate our asymptotic results only for the case of a circular landscape where the predator has a centralizing tendency towards the origin.

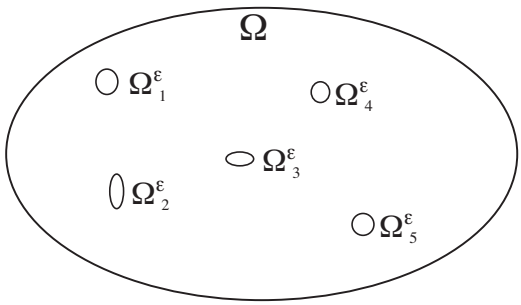

Fig. 1 A schematic plot of the landscape Ω with five small prey patches.

2.1 Asymptotic Solution for the MFPT With Drift

In this section we consider (2.2) for the MFPT allowing for the presence of drift. This problem is solved asymptotically by the method of matched asymptotic expansions (cf. [29]). Related problems involving elliptic PDE's in perforated 2-D domains with no drift have been studied in [9, 13, 30, 39, 47, 52, 55].

Following [52], the outer expansion away from the prey patches is taken to have the form

$$u \sim U_0(\mathbf{x}, \boldsymbol{\nu}) + \sigma(\varepsilon) U_1(\mathbf{x}, \nu) + \cdots . \tag{2.3}$$

Here $\boldsymbol{\nu} \equiv (\nu_1, \ldots, \nu_N)$ is defined in terms of the logarithmic gauge functions $\nu_j \equiv -1/\log(\varepsilon d_j)$ for $j = 1, \ldots, N$. As shown below, the constant d_j is obtained from a certain canonical inner problem defined near the j-th patch. In the outer expansion, the correction term $\sigma(\varepsilon)$ is assumed to satisfy $\sigma(\varepsilon) \ll \nu_j^k$ for each $j = 1, \ldots, N$, and for any positive power k, so that the correction term induced by U_1 is beyond-all-orders with respect to all of the logarithmic terms captured by U_0. Upon substituting (2.3) into (2.2), we obtain that U_0 satisfies

$$\Delta U_0 + \nabla\psi \cdot \nabla U_0 = -1\,, \quad \mathbf{x} \in \Omega \setminus \{\mathbf{x}_1, \ldots, \mathbf{x}_N\}\,; \qquad \frac{\partial U_0}{\partial n} = 0\,, \quad \mathbf{x} \in \partial\Omega\,. \tag{2.4}$$

Since the patches shrink to the points $\mathbf{x}_j \in \Omega$ as $\varepsilon \to 0$ for $j = 1, \ldots, N$, this outer problem for U_0 must be supplemented by appropriate singularity conditions as $\mathbf{x} \to \mathbf{x}_j$, for each $j = 1, \ldots, N$. These singularity conditions are derived below by matching the outer expansion to an inner expansion that is constructed near each of the N patches.

For the inner problem near the j-th patch, we define an inner variable $\mathbf{y} = \varepsilon^{-1}(\mathbf{x} - \mathbf{x}_j)$ and the corresponding magnified patch Ω_j by $\Omega_j = \varepsilon^{-1}\Omega_j^\varepsilon$. Near the j-th patch, we introduce the inner solution q_j by $q_j(\mathbf{y}) = u(\mathbf{x}_j + \varepsilon\mathbf{y})$, and we pose the inner expansion

$$q_j \sim \nu_j \gamma_j(\boldsymbol{\nu}) q_{0j}(\mathbf{y}) + \alpha(\varepsilon, \boldsymbol{\nu}) q_{1j}(\mathbf{y}) + \cdots . \tag{2.5}$$

Here γ_j is an unknown constant to be determined. The gauge function α is assumed to be beyond-all-orders with respect to the logarithmic terms, and so satisfies $\alpha \ll \nu_j^k$ for any positive integer k as $\varepsilon \to 0$. We impose that q_{0j} grows logarithmically at infinity, and from the original PDE (2.2) for the MFPT we obtain that q_{0j} satisfies

$$\begin{aligned} &\Delta_{\mathbf{y}} q_{0j} = 0\,, \quad \mathbf{y} \notin \Omega_j\,; \qquad q_{0j} = 0\,, \quad \mathbf{y} \in \partial\Omega_j\,, \\ &\quad q_{0j} \sim \log|\mathbf{y}| - \log d_j + \mathcal{O}(|\mathbf{y}|^{-1})\,, \quad \text{as} \quad |\mathbf{y}| \to \infty\,. \end{aligned} \tag{2.6}$$

We remark that the behavior $q_{0j} \sim \log|\mathbf{y}|$ as $|\mathbf{y}| \to \infty$ is sufficient to determine the solution for q_{0j} uniquely. In terms of this solution, the $\mathcal{O}(1)$ term in the far-field behavior, is uniquely determined. The $\mathcal{O}(|\mathbf{y}|^{-1})$ unspecified term is the dipole term in the far-field behavior. The constant d_j is known as the logarithmic capacitance (cf. [40]) of Ω_j and it depends on the shape of Ω_j but not on its orientation. Numerical values for d_j for different shapes of Ω_j are given in [40], and some of

Shape of $\Omega_j \equiv \varepsilon^{-1}\Omega_j^\varepsilon$	Logarithmic capacitance d_j
circle, radius a	$d_j = a$
ellipse, semi-axes a, b	$d_j = \frac{a+b}{2}$
equilateral triangle, sidelength h	$d_j = \frac{\sqrt{3}\,\Gamma\left(\frac{1}{3}\right)^3 h}{8\pi^2} \approx 0.422h$
isosceles right triangle, short side h	$d_j = \frac{3^{3/4}\Gamma\left(\frac{1}{4}\right)^2 h}{2^{7/2}\pi^{3/2}} \approx 0.476h$
square, sidelength h	$d_j = \frac{\Gamma\left(\frac{1}{4}\right)^2 h}{4\pi^{3/2}} \approx 0.5902h$

Table 1 The logarithmic capacitance d_j for some cross-sectional shapes of $\Omega_j \equiv \varepsilon^{-1}\Omega_j^\varepsilon$.

these are reproduced in Table 1. A boundary integral method to numerically compute d_j for an arbitrarily-shaped domain Ω_j is described and implemented in [14].

Upon substituting the far-field behavior of q_{0j} as $|\mathbf{y}| \to \infty$ into (2.5), and re-writing the result in terms of the outer variable, we obtain from the matching condition that the outer solution U_0 must have the following singularity structure:

$$U_0(\mathbf{x}, \boldsymbol{\nu}) \sim \nu_j \gamma_j \log|\mathbf{x} - \mathbf{x}_j| + \gamma_j\,, \quad \text{as} \quad \mathbf{x} \to \mathbf{x}_j\,, \qquad j = 1, \ldots, N\,. \tag{2.7}$$

For each $j = 1, \ldots, N$, (2.7) specifies both the regular and singular part of the outer solution. As such, for each $j = 1, \ldots, N$, we have one constraint for the determination of the γ_j for $j = 1, \ldots, N$. Overall, these constraints will lead to a linear algebraic system for the unknown γ_j for $j = 1, \ldots, N$.

The outer problem (2.4) for U_0 can be defined in Ω by introducing singular Dirac delta function forces and by re-writing the system in divergence form by introducing $P(\mathbf{x})$ by $P = e^{\psi}$. In this way, (2.4) can be re-written as

$$\nabla \cdot (P\nabla U_0) = -P + 2\pi P \sum_{k=1}^{N} \nu_k \gamma_k \delta(\mathbf{x} - \mathbf{x}_k)\,, \quad \mathbf{x} \in \Omega\,; \qquad \frac{\partial U}{\partial n} = 0\,, \quad \mathbf{x} \in \partial\Omega\,, \tag{2.8}$$

where U_0 must satisfy the singularity behavior (2.7). By applying the divergence theorem to (2.8), we must have that

$$2\pi \sum_{k=1}^{N} P(\mathbf{x}_k)\nu_k\gamma_k = \int_\Omega P(\mathbf{x})\,d\mathbf{x}\,. \tag{2.9}$$

Next, we decompose U_0 in terms of a smooth function $U_{0H}(\mathbf{x})$ and a sum of Green's functions in the form

$$U_0 = U_{0H} + 2\pi \sum_{k=1}^{N} \nu_k \gamma_k G(\mathbf{x}; \mathbf{x}_k) + \chi\,. \tag{2.10}$$

Here χ is an arbitrary constant, and the smooth part U_{OH} is taken to satisfy

$$\nabla \cdot (P\nabla U_{0H}) = -P + P_{\text{ave}}\,, \quad \mathbf{x} \in \Omega\,; \qquad \frac{\partial U_{0H}}{\partial n} = 0\,, \quad \mathbf{x} \in \partial\Omega\,; \qquad \int_\Omega U_{0H}\,d\mathbf{x} = 0\,. \tag{2.11}$$

Here P_{ave} is the average of P over Ω, defined explicitly by

$$P_{\text{ave}} \equiv \frac{1}{|\Omega|}\int_\Omega P(\mathbf{x})\,d\mathbf{x}\,. \tag{2.12}$$

where $|\Omega|$ is the area of Ω. The zero average condition on U_{0H} in (2.11) ensures that U_{0H} is uniquely determined.

In (2.10), the Green's function $G(\mathbf{x}; \boldsymbol{\xi})$ is the unique solution to

$$\begin{aligned} \nabla \cdot (P\nabla G(\mathbf{x}; \boldsymbol{\xi})) = -\frac{P(\boldsymbol{\xi})}{|\Omega|} + P(\mathbf{x})\delta(\mathbf{x} - \boldsymbol{\xi})\,, \quad \mathbf{x} \in \Omega\,; \qquad \frac{\partial G}{\partial n} = 0\,, \quad \mathbf{x} \in \partial\Omega\,, \\ G \sim \frac{1}{2\pi}(\log|\mathbf{x} - \boldsymbol{\xi}| + R(\boldsymbol{\xi})) + o(1) \quad \text{as} \quad \mathbf{x} \to \boldsymbol{\xi}\,; \qquad \int_\Omega G(\mathbf{x}; \boldsymbol{\xi})\,d\mathbf{x} = 0\,. \end{aligned} \tag{2.13}$$

Here $R(\boldsymbol{\xi})$ is called the regular part of the Green's function. When there is no drift, corresponding to $P \equiv 1$, $R(\boldsymbol{\xi})$ can be found analytically when Ω is either a disk or rectangle (cf. [30], [39]). For arbitrary domains, $G(\mathbf{x};\boldsymbol{\xi})$ and $R(\boldsymbol{\xi})$ must be computed numerically. Finally, in (2.10), the unknown constant χ can be interpreted as

$$\chi = \frac{1}{|\Omega|}\int_{\Omega} U_0(\mathbf{x})d\mathbf{x}\,. \tag{2.14}$$

To determine the linear algebraic system for γ_j, we expand the solution in (2.10) as $\mathbf{x}\to\mathbf{x}_j$ and equate the resulting expression with the required singular behavior in (2.7). This leads to

$$U_{0H}(\mathbf{x}_j) + 2\pi\sum_{k=1,k\neq j}^{N}\nu_k\gamma_k G(\mathbf{x}_k;\mathbf{x}_j) + \nu_j\gamma_j\left(\log|\mathbf{x}-\mathbf{x}_j| + R(\mathbf{x}_j)\right) + \chi \sim \nu_j\gamma_j\log|\mathbf{x}-\mathbf{x}_j| + \gamma_j\,.$$

In this expression, the logarithmic terms in $|\mathbf{x}-\mathbf{x}_j|$ agree identically (as they should), and from the non-singular terms we obtain a linear algebraic system for the γ_j for $j=1,\ldots,N$. We summarize our result in the following statement.

Principal Result 2.1: (Drift) *For $\varepsilon \ll 1$, the asymptotic solution for the MFPT (2.2) in the outer region is given by*

$$u \sim U_{0H} + 2\pi\sum_{j=1}^{N}\nu_j\gamma_j G(\mathbf{x};\mathbf{x}_j) + \chi\,, \tag{2.15a}$$

where the γ_j for $j=1,\ldots,N$ and the constant χ are the solution to the $N+1$ dimensional linear algebraic system consisting of the N equations

$$\gamma_j\left(\nu_j R(\mathbf{x}_j) - 1\right) + 2\pi\sum_{k=1,k\neq j}^{N}\nu_k\gamma_k G(\mathbf{x}_j;\mathbf{x}_k) + \chi = -U_{0H}(\mathbf{x}_j)\,, \qquad j=1,\ldots,N\,, \tag{2.15b}$$

coupled to the constraint

$$2\pi\sum_{k=1}^{N}P(\mathbf{x}_k)\nu_k\gamma_k = \int_{\Omega}P(\mathbf{x})\,d\mathbf{x}\,. \tag{2.15c}$$

Here $P=e^{\psi}$, $\nu_j = -1/\log(\varepsilon d_j)$, where d_j is the logarithmic capacitance of Ω_j defined by the solution to (2.6), U_{0H} is the smooth solution satisfying (2.11), and the Green's function G with regular part R satisfy (2.13).

The linear system in Principal Result 2.1 is asymptotically diagonally dominant when $\nu_{\max} = \max_j \nu_j$ is sufficiently small, and so is uniquely solvable when $\nu_{\max}$ is small enough. This system incorporates all of the logarithmic gauge functions in the asymptotic solution for the MFPT, leaving an error term that is beyond-all-orders in $(-1/\log(\varepsilon d_j))^k$. This error term, which we do not calculate here, arises from the local gradient behavior of G as $\mathbf{x}\to\mathbf{x}_j$ as well as from the dipole far-field behavior of the canonical inner solution (2.6). An advantage of the hybrid method over the traditional method of matched asymptotic expansions (cf. [29]) is that the hybrid formulation is able to effectively "sum" an infinite series of logarithmic gauge functions, thereby providing a highly accurate approximate solution.

In the absence of drift, for which $P=1$ for $\mathbf{x}\in\Omega$, Principal Result 2.1 can be simplified as follows:

Principal Result 2.2: (No Drift) *For $\varepsilon \ll 1$, and in the absence of drift for which $P\equiv 1$, the asymptotic solution for the MFPT (2.2) in the outer region is given by*

$$u \sim 2\pi\sum_{j=1}^{N}\nu_j\gamma_j G_0(\mathbf{x};\mathbf{x}_j) + \chi\,, \tag{2.16a}$$

where the γ_j for $j=1,\ldots,N$ and the constant χ are the solution to the $N+1$ dimensional linear algebraic system

$$\gamma_j\left(\nu_j R_0(\mathbf{x}_j) - 1\right) + 2\pi\sum_{k=1,k\neq j}^{N}\nu_k\gamma_k G_0(\mathbf{x}_j;\mathbf{x}_k) + \chi = 0\,, \quad j=1,\ldots,N\,; \qquad 2\pi\sum_{j=1}^{N}\nu_j\gamma_j = |\Omega|\,. \tag{2.16b}$$

Here $\nu_j = -1/\log(\varepsilon d_j)$, d_j is the logarithmic capacitance associated with the j-th prey patch Ω_j, as defined by (2.6), while G_0 is the Neumann Green's function with regular part R_0 satisfying

$$\begin{aligned} &\Delta G_0(\mathbf{x};\boldsymbol{\xi}) = -\frac{1}{|\Omega|} + \delta(\mathbf{x}-\boldsymbol{\xi})\,, \quad \mathbf{x}\in\Omega\,; \qquad \frac{\partial G_0}{\partial n} = 0\,, \quad \mathbf{x}\in\partial\Omega\,, \\ &G_0 \sim \frac{1}{2\pi}(\log|\mathbf{x}-\boldsymbol{\xi}| + R_0(\boldsymbol{\xi})) + o(1)\,, \quad \text{as} \quad \mathbf{x}\to\boldsymbol{\xi}\,; \qquad \int_\Omega G_0(\mathbf{x};\boldsymbol{\xi})\,d\mathbf{x} = 0\,. \end{aligned} \tag{2.17}$$

For an arbitrary domain, G_0 and R_0 must be computed numerically. However, when Ω is the unit disk, and upon identifying $\mathbf{x}$ and $\boldsymbol{\xi}$ as points in complex notation inside the unit disk, it is well-known that (cf. [30])

$$G_0(\mathbf{x};\boldsymbol{\xi}) = \frac{1}{2\pi}\left(\log|\mathbf{x}-\boldsymbol{\xi}| + \log\left|\mathbf{x}|\boldsymbol{\xi}| - \frac{\boldsymbol{\xi}}{|\boldsymbol{\xi}|}\right| - \frac{1}{2}(|\mathbf{x}|^2+|\boldsymbol{\xi}|^2) + \frac{3}{4}\right)\,, \qquad R_0(\boldsymbol{\xi}) = \log\left(1-|\boldsymbol{\xi}|^2\right) - |\boldsymbol{\xi}|^2 + \frac{3}{4}\,. \tag{2.18}$$

We remark that the analysis leading to Principal Result 2.1 has assumed that $|\mathbf{x}_i - \mathbf{x}_j| = \mathcal{O}(1)$ for any $i \neq j$. In §5.3 below, we show how to modify Principal Result 2.1 to analyze the case where two patches are $\mathcal{O}(\varepsilon)$ close.

In general, for a given drift function and arbitrary landscape, the Green's function, its regular part, and the function U_{0H} must be computed numerically in order to implement the asymptotic result in Principal Results 2.1 and 2.2. Although the Green's function depends on both the drift and the centers of the prey-patches, it is independent of the effective radius ε and the specific shapes of the prey patches. The effect of both the radii and shape of the prey patches are analytically encoded in (2.15) through the products εd_j for $j = 1\ldots, N$. The logarithmic capacitances d_j are known analytically for various prey patch shapes, and can be pre-computed by a boundary integral method for arbitrary shapes. In this way, if either the size or shape of any of the prey patches is altered, all that is required to implement the hybrid formulation is to simply change the logarithmic capacitance d_j for that particular prey patch, while still retaining the same pre-computed Green's function and function U_{0H}. Then, by numerically solving a simple linear system, we can readily compute the MFPT over a full range of ε. In contrast, from the viewpoint of a direct full numerical solution of the PDE (2.2), a different fine-scale numerical discretization would be required to compute the MFPT for each specific collection of patch shapes and sizes. Changing either the effective radius ε or shape of any one of the prey patches would require a new discretization of the PDE (2.2). Finally, we remark that with our hybrid approach we have avoided the difficulty and loss of solution accuracy associated with inverting the numerically ill-conditioned large linear algebraic system arising from the discretization of the full PDE at small ε. This numerical ill-conditioning results from an eigenvalue of the underlying matrix problem that tends to zero as $\varepsilon \to 0$, which is proportional to the reciprocal of the MFPT.

3 Numerical Verification for the MFPT With and Without Drift

We now compare numerical results obtained from our asymptotic analysis with full numerical results obtained by solving the PDE (2.2) for the MFPT directly using the finite element software package FlexPDE6 [16]. We remark that all full PDE computations in this paper are done using this software. Although our asymptotic analysis is valid for any arbitrary-shaped landscape and arbitrary patch shapes, for simplicity, we will only compare asymptotic and numerical results for a circular-shaped landscape Ω with circular-shaped prey patches. In the numerical comparisons below, Ω is taken to have radius $L = 1$ km. In most of our computations below, the prey patches are taken to be circles of radius 0.0067 km as suggested in [35]. This leads to a non-dimensional prey-patch radius of $\varepsilon = 0.0067$. In terms of the solution u to the non-dimensional PDE, the dimensional MFPT T is given by $T = L^2 u/D_{\rm dim}$. We use the value $D_{\rm dim} = 0.41{\rm km}^2/{\rm hr}$ from [35] as an estimate of the diffusivity of the predator.

In the absence of drift, the asymptotic and full numerical results for the dimensional average MFPT, $T_{\rm ave}$, assuming a uniform distribution of starting points in the unit disk, is

$$T_{\rm asy} \equiv \chi/0.41\,, \qquad T_{\rm num} \equiv \frac{1}{0.41|\Omega\backslash\Omega_p|}\int_{\Omega\backslash\Omega_p} u(\mathbf{x})\,d\mathbf{x}\,, \tag{3.1}$$

where Ω is the unit disk, Ω_p is the union of the prey patches, u solves (2.2) with $\psi = 0$, and χ is found from (2.16).

We first study the effect of the location of a single circular patch of radius $\varepsilon = 0.0067$ on the MFPT of the predator. In Fig. 2 we show a very favorable comparison between the asymptotic average MFPT and the corresponding full numerical result as the patch moves away from the center of the unit disk. We observe that the average MFPT increases with the distance of the patch from the center of the disk. The reason for this increase is that as the patch moves away from the center of the disk, its average distance from all the points in the domain increases. Hence, the farther the patch is from the center of the domain, the less reachable it is, and so the average MFPT must increase.

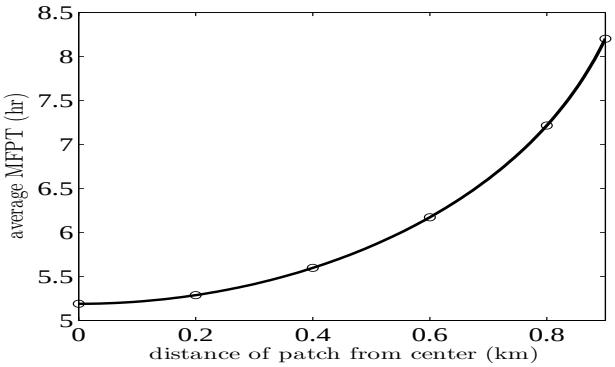

Fig. 2 For the case of no drift, and for one circular prey patch of radius $\varepsilon = 0.0067$, the spatial average of the MFPT obtained from Principal Result 2.2 (solid curve) is compared with the corresponding full numerical result (open circles) computed from the PDE (2.2). The horizontal axis is the distance of the prey patch from the center of the unit disk.

Next, still assuming no drift, we compare results from our asymptotic analysis with corresponding full numerical results for the case of three circular patches of a common radius $\varepsilon = 0.0067$ inside the unit disk. We consider two realizations of this configuration, corresponding to different locations of the three patches. The specific locations of the prey patches, together with a very favorable comparison between the asymptotic and full numerical results for the dimensional average MFPT are shown in Table 2.

Patch1	Patch2	Patch3	avg. MFPT (hr) (asy)	avg. MFPT (hr) (num)
(0.5,0.3)	(-0.2,0.6)	(-0.4,-0.7)	1.6881	1.6878
(0.3,0.8)	(0.1,-0.6)	(-0.5,-0.7)	1.9936	1.9921

Table 2 Spatial averages of the dimensional MFPT, assuming no drift, for two different three-patch configurations in the unit disk Ω. All patches have radii $\varepsilon = 0.0067$ and we use $D_{\text{dim}} = 0.41\text{km}^2/\text{hr}$. The asymptotic and numerical results are given in (3.1).

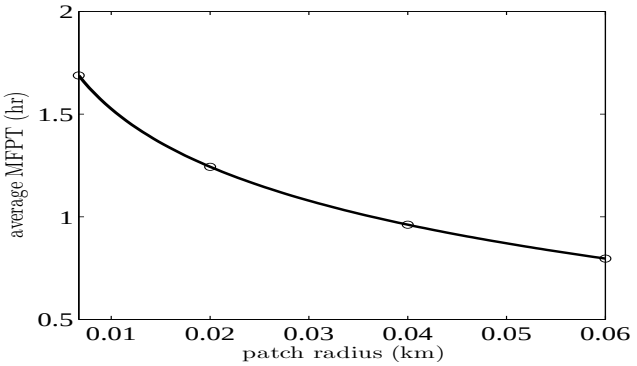

Fig. 3 For no drift, and for a three-patch configuration with circular patches centered at $(0.5, 0.3)$, $(-0.2, 0.6)$, and $(-0.4, -0.7)$, the asymptotic (solid curve) and full numerical results (open circles) for the dimensional average MFPT are compared as the common patch radius ε increases. The asymptotic and full numerical results are still rather close even when $\varepsilon \approx 0.06$.

For the three-patch configuration of the first row of Table 2, Fig. 3 shows that the asymptotic result for the dimensional average MFPT is still in very close agreement with the corresponding full numerical result on the range $0.0067 < \varepsilon < 0.06$ of the common circular prey patch radius ε. This suggests that the asymptotic results of Principal Result 2.2 can still be used at only moderately small values of ε.

3.1 Numerical Verification for the MFPT With Drift

Next, allowing for a drift term, we compare asymptotic results obtained from Principal Result 2.1 with corresponding full numerical results computed from (2.2) using FlexPDE6 [16]. We take Ω to be a circular landscape of radius $L = 1$km, we fix $D = D_{\rm dim} = 0.41\text{km}^2/\text{hr}$, and assume as in [35] that there is a drift term $c(\mathbf{X})$ directed towards the origin with magnitude 0.085km/hr. This gives the predator a centralizing tendency to its den-site at the center of the landscape Ω. The corresponding non-dimensional ψ in (2.2) has the form

$$\psi = -\beta|\mathbf{x}|\,, \qquad \beta \equiv \frac{c_0 L}{D_{\rm dim}} = \frac{0.085}{0.41} \approx 0.207317073\,. \tag{3.2}$$

We refer below to β as the drift parameter, as it measures the relative effect of the centralizing tendency of the predator to the isotropic diffusivity D associated with a pure Brownian motion of the predator.

Since the predator has a centralizing tendency, it is not reasonable to assume that the initial probability distribution $S(\mathbf{X})$ of starting points in Ω is uniformly distributed in Ω as for the case with no drift. Instead, as shown in [35], the dimensional $S(\mathbf{X})$ is given by the steady-state of the Kolmogorov equation

$$\frac{\partial S}{\partial t} = \nabla' \cdot \mathbf{J}\,, \qquad \mathbf{J} \equiv D\nabla' S - \mathbf{c}(\mathbf{X})S\,, \qquad \mathbf{X} \in \Omega\,; \qquad \mathbf{J}\cdot\hat{\mathbf{n}} = 0\,, \quad \mathbf{X} \in \partial\Omega\,; \qquad \int_\Omega S\, d\mathbf{X} = 1\,, \tag{3.3}$$

where the primes indicate derivatives with respect to the dimensional variable $\mathbf{X}$. Here $c(\mathbf{X}) = -c_0\mathbf{X}/|\mathbf{X}|$, $\hat{\mathbf{n}}$ is the unit outward normal to Ω, and the boundary condition on $\partial\Omega$ models a reflective outer boundary (cf. [18]). In terms of $S(\mathbf{X})$ and the dimensional MFPT T, the distributional average of the MFPT over all possible starting points in Ω is defined by

$$T_{\rm avg} \equiv \int_{\Omega\setminus\Omega_p} S(\mathbf{X})T(\mathbf{X})\, d\mathbf{X}\,, \tag{3.4}$$

where Ω_p is the union of all the prey patches. Full numerical results for $T_{\rm avg}$ are obtained by first solving the full PDE (2.2) numerically with FlexPDE6 [16], and then employing a numerical quadrature to calculate the integral in (3.4).

When Ω is the unit disk, the steady-state solution of (3.3) is radially symmetric and can be found analytically. In terms of a dimensionless polar coordinate system, (3.3) readily reduces to

$$S_{rr} + \frac{1}{r}S_r + \frac{\beta}{r}\frac{\partial}{\partial r}(rS) = 0\,, \quad 0 < r < 1\,; \qquad S_r + \beta S = 0\,, \quad \text{on} \quad r = 1\,; \qquad \beta \equiv \frac{c_0}{D_{\rm dim}}\,.$$

A first integral of the equation for S yields $S_r + \beta S = k_1/r$, for some constant k_1. By imposing the reflective boundary condition on $r = 1$ we get $k_1 = 0$, so that $S = S_0 e^{-\beta r}$ for some constant S_0. The constant S_0 is found from the integral constraint $\int_0^1 rS\, dr = 1/(2\pi)$. In this way, $S(r)$ is given explicitly by

$$S(r) = S_0 e^{-\beta r}\,, \qquad S_0 = \frac{1}{2\pi}\left[\int_0^1 re^{-\beta r}\, dr\right]^{-1} = \frac{1}{2\pi}\left[\frac{1}{\beta^2}\left(1 - e^{-\beta}\right) - \frac{e^{-\beta}}{\beta}\right]^{-1}\,. \tag{3.5}$$

Therefore, S is bounded in Ω but is not smooth at $r = 0$. In the limit $\beta \to 0$ of small drift, (3.5) yields that $S \to 1/\pi$, which corresponds to the uniform distribution in the unit disk. In Fig. 4 we plot $S(r)$ versus r for the β as given in (3.2) and for ten times this value, which corresponds to a ten times larger drift velocity magnitude.

The corresponding asymptotic result for the prediction of $T_{\rm avg}$ is obtained by neglecting the $\mathcal{O}(\varepsilon^2)$ contribution of Ω_p in (3.4), and by using the outer solution for T in the integral, so that $T \approx u/D_{\rm dim}$ where u is given in (2.15a). In order to determine this outer solution u, we must numerically implement (2.15) of Principal Result 2.1. This involves first calculating U_{0H} from (2.11) as well as numerically computing the Green's function and its regular part as defined in (2.13). In terms of these quantities, the linear algebraic system in (2.15) is then solved numerically, which determines the outer approximation for the non-dimensional MFPT u from (2.15a).

To determine U_{0H} when Ω is the unit disk with a centralizing drift term, we substitute $P = e^{-\beta|\mathbf{x}|}$ into (2.11) with $r = |\mathbf{x}|$ to obtain that the radially symmetric function $U_{0H}(r)$ satisfies

$$U_{0H}'' + \left(\frac{1}{r} - \beta\right)U_{0H}' = -1 + P_{\rm ave}e^{\beta r}\,, \qquad P_{\rm ave} \equiv 2\int_0^1 re^{-\beta r}\, dr = 2\left[\frac{1}{\beta^2} - e^{-\beta}\left(\frac{1}{\beta^2} + \frac{1}{\beta}\right)\right]\,. \tag{3.6}$$

We integrate (3.6) and impose $U_{0H}'(1) = 0$. A further integration then yields the explicit expression

$$U_{0H}(r) = \frac{P_{\rm ave}}{2}\left[\frac{re^{\beta r}}{\beta} - \frac{e^{\beta r}}{\beta^2} + \frac{1}{\beta^2}\right] + \frac{1}{\beta^2}\int_0^r \frac{\left(1 - e^{\beta\rho}\right)}{\rho}\, d\rho + \frac{r}{\beta} + U_{0H}(0)\,, \tag{3.7a}$$

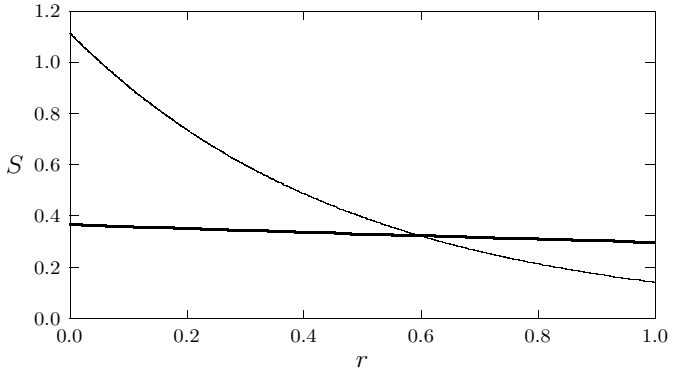

Fig. 4 Plot of the steady-state solution $S(r)$ to (3.3) in the unit disk, as obtained from (3.5), which gives the probability distribution of initial starting points for the predator under a central drift. The heavy solid curve is for β as given in (3.2), while the solid curve is for $\beta \approx 2.07317073$, representing a drift magnitude that is ten times larger.

with the constant $U_{0H}(0)$ determined from the requirement that $\int_0^1 rU_{0H}(r)\,dr = 0$. For the drift velocity magnitude of [35], and for a factor of ten times this value as also used below, a simple numerical quadrature determines $U_{0H}(0)$ as

$$U_{0H}(0) \approx 0.0078943\,, \quad \text{when} \quad \beta \approx 0.207317073\,; \qquad U_{0H}(0) \approx 0.072267\,, \quad \text{when} \quad \beta \approx 2.07317073\,. \tag{3.7b}$$

To compute the Green's function numerically from (2.13) we decompose $G(\mathbf{x};\boldsymbol{\xi})$ into a sum of a regular part and the appropriate logarithmic singularity given by (2.13). That is, we let

$$G(\mathbf{x};\boldsymbol{\xi}) = \frac{1}{2\pi}\left(\log|\mathbf{x}-\boldsymbol{\xi}| + R(\mathbf{x};\boldsymbol{\xi})\right)\,. \tag{3.8}$$

Substituting (3.8) into (2.13), and noting that $\Delta \log|\mathbf{x}-\boldsymbol{\xi}| = 2\pi\delta(\mathbf{x}-\boldsymbol{\xi})$, we find that $R(\mathbf{x};\boldsymbol{\xi})$ satisfies

$$\begin{aligned} &\nabla\cdot(P\nabla R) = -\frac{2\pi}{|\Omega|}P(\boldsymbol{\xi}) - \nabla P(\mathbf{x})\cdot\nabla\log|\mathbf{x}-\boldsymbol{\xi}|\,, \quad \mathbf{x}\in\Omega\,; \\ &\partial_n R = -\partial_n\log|\mathbf{x}-\boldsymbol{\xi}|\,, \quad \mathbf{x}\in\partial\Omega\,; \qquad \int_\Omega R(\mathbf{x};\boldsymbol{\xi})\,d\mathbf{x} = -\int_\Omega \log|\mathbf{x}-\boldsymbol{\xi}|\,d\mathbf{x}\,. \end{aligned} \tag{3.9}$$

In this way, the solution for the Green's function may be obtained from (3.8) by numerically solving the regular problem (3.9) using FlexPDE6 [16]. The regular part $R(\boldsymbol{\xi})$, defined in (2.13), is then given by $R(\boldsymbol{\xi}) = R(\boldsymbol{\xi};\boldsymbol{\xi})$. A key feature of FlexPDE6 is that integral constraints, such as in (3.9), on the solution to a PDE can readily be imposed.

We now give some asymptotic and numerical results for several configurations of prey patches under the effect of a centralizing drift. We first study the effect of the location of a circular prey patch of radius $\varepsilon = 0.0067$ in the unit disk Ω on the distributional average of the MFPT for the predator. The results for various patch locations, as displayed in Fig. 5, show a very close agreement between the asymptotic and full numerical results. Similar to the case without drift, the distributional average of the MFPT increases with the distance of the patch from the center of the disk.

Next, we compare asymptotic and full numerical results for the distributional average of the MFPT when the unit disk contains three circular patches each of radius $\varepsilon = 0.0067$. The drift parameter is $\beta = 0.085/0.41$. Two configurations of three patches are considered. The results in Table 3 show a remarkably close agreement between the asymptotic and full numerical results. A grey-scale 2-D plot of the full numerical result for the MFPT corresponding to the second configuration of patches in Table 3 and for $\varepsilon = 0.0067$ is shown in the left panel of Fig. 6. In the right panel of Fig. 6 we compare the asymptotic and full numerical results for the distributional average of the MFPT on the range $0.0067 < \varepsilon < 0.06$. We observe that the asymptotic result is still very close to the full numerical result at the larger prey patch radius $\varepsilon = 0.06$.

Next, we compare the distributional average of the MFPT with and without the drift term. We recall that since $S \to 1/\pi$ as $\beta \to 0$, the distributional average of the MFPT tends as $\beta \to 0$ to the average MFPT, which assumes a uniform distribution of starting points in Ω. We will consider a single circular prey patch of radius $\varepsilon = 0.0067$, where the distance of the prey patch to the boundary of the circular landscape is allowed to vary.

As shown in the left panel of Fig. 7, when the centralizing drift velocity has magnitude 0.085 km/hr, so that $\beta = 0.085/0.41$, there is only a slight difference between the asymptotic results for the distributional average of the MFPT

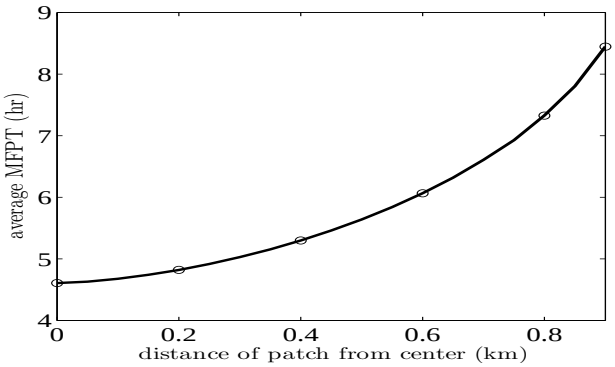

Fig. 5 Distribution averages T_{avg} of the asymptotic and full numerical results for the MFPT are plotted versus the distance of a prey patch from the center of the circular disk. The circular prey patch has radius $\varepsilon = 0.0067$ and $\beta = 0.085/0.41$ as in (3.2).

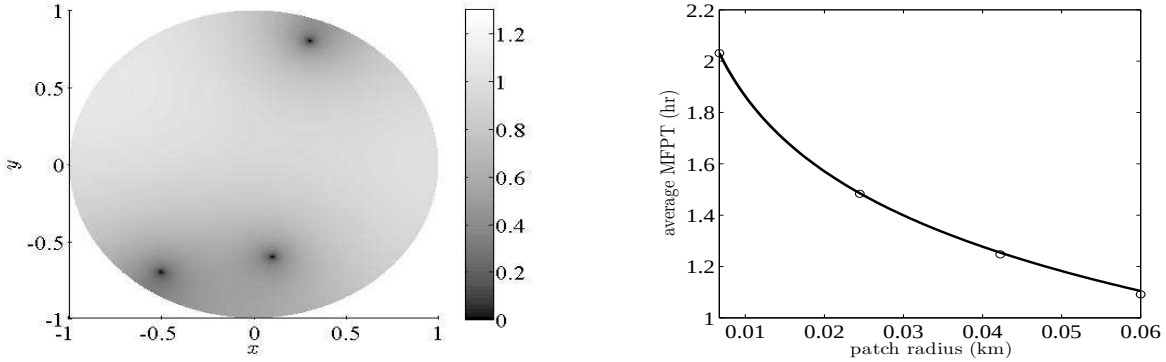

Fig. 6 MFPT (left panel) and the distributional average of the MFPT (right panel) for three circular patches of prey of radius $\varepsilon = 0.0067$ centered at $(0.3, 0.8)$, $(0.1, -0.6)$, and $(-0.5, -0.7)$. The drift parameter is $\beta = 0.085/0.41$. Left panel: full numerical result for the MFPT when $\varepsilon = 0.0067$. Right panel: comparison of the asymptotic (solid curve) and full numerical results (open circles) for the distributional average of the MFPT as a function of the common prey patch radius ε on the range $0.0067 < \varepsilon < 0.06$. The agreement between the asymptotic and full numerical results is close even at these larger values of ε.

Patch1	Patch2	Patch3	T_{avg} (hr) (asy)	T_{avg} (hr) (num)
(0.5,0.3)	(-0.2,0.6)	(-0.4,-0.7)	1.6916	1.6916
(0.3,0.8)	(0.1,-0.6)	(-0.5,-0.7)	2.0312	2.0311

Table 3 Distributional average (see (3.4)) of the MFPT for a unit disk containing three circular patches of radius $\varepsilon = 0.0067$ and with drift parameter $\beta = 0.085/0.41$. The asymptotic result is obtained from Principal Result 2.1 and the full numerical result is computed from (2.2).

with and without drift. However, when the magnitude of the drift velocity is increased by a factor of 10 to 0.85 km/hr, so that $\beta = 0.85/0.41 \approx 2.07317073$, in the right panel of Fig. 7 we show an interesting cross-over effect between the distributional average of the MFPT with and without drift. From this figure we observe that with larger drift and a centralizing tendency, the distributional average of the MFPT is significantly smaller for prey patches near the origin than for the case of pure Brownian motion. However, as the prey patch moves towards the edge of the unit disk, the average MFPT with drift increases rather noticeably and eventually surpasses the no-drift MFPT result. Intuitively, this suggests that denning animals, which have a centralizing tendency, have a significantly larger search time when the prey is located farther from the den. Moreover, it also suggests that for a given drift magnitude, pure diffusive motion leads to a lower average MFPT than motion under a centralizing drift when the prey patch is sufficiently far from the den.

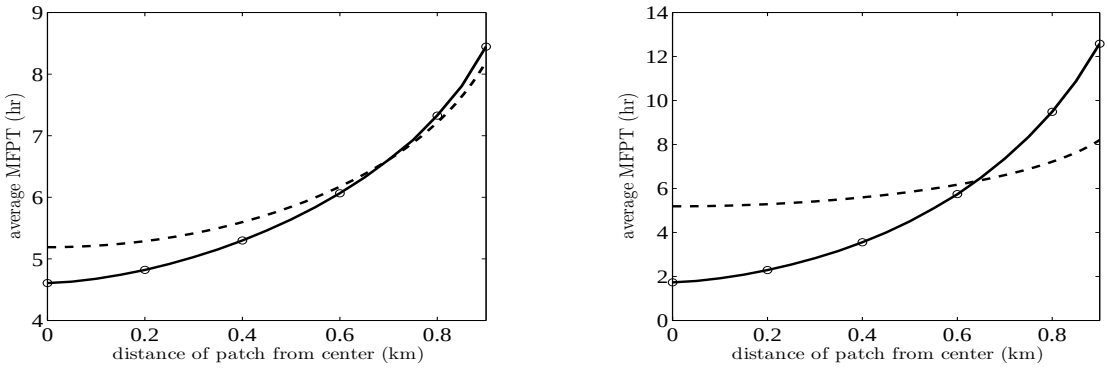

Fig. 7 Left panel: Distributional average of the MFPT with drift (solid curve) and without drift (dotted curve), as obtained from Principal Results 2.1 and 2.2 respectively, are plotted versus the distance of the center of a circular prey patch of radius $\varepsilon = 0.0067$ from the center of the disk. Here the drift velocity magnitude is 0.085 km/hr, so that $\beta = 0.085/0.41 \approx 0.207317$. The open circles are the full numerical results computed from the PDE. Right panel: same plot but for a ten times larger drift parameter value of $\beta = 0.85/0.41 \approx 2.07317$. The dotted curve, representing no drift, was favorably compared with full numerics in Fig. 2.

4 The MFPT with Variable Diffusivity

In any habitat, the presence of terrestrial inhomogeneities like hills, mountains, lowlands, marshes, and rivers can affect animal movement in the habitat. The simplest model of the mean first passage time that accounts for these inhomogeneities in the landscape is to allow for a variable, but isotropic, diffusivity in the PDE for the MFPT without drift. In this section we show how the previous MFPT analysis can be modified to allow for an arbitrary variable diffusivity D in an arbitrary 2-D domain. The non-dimensional PDE for the MFPT can be written as

$$\Delta u(\mathbf{x}) = -1/D(\mathbf{x})\,, \quad \mathbf{x} \in \Omega \setminus \cup_{j=1}^{N} \Omega_j^{\varepsilon}\,; \qquad \frac{\partial u}{\partial n} = 0\,, \quad \mathbf{x} \in \partial\Omega\,; \qquad u = 0\,, \quad \mathbf{x} \in \partial\Omega_j^{\varepsilon}\,, \quad j = 1, \ldots, N\,. \tag{4.1}$$

The problem is similar to the one without drift analyzed in §2.1, with the only difference being that the diffusivity D here is spatially dependent. As such, since the analysis needed to analyze (4.1) is similar to that for the case with constant diffusivity, we will only give the main result obtained from an asymptotic analysis of (4.1).

Principal Result 4.1: (Variable Diffusivity) *For $\varepsilon \ll 1$, the asymptotic solution for the MFPT (4.1) in the outer region is given by*

$$u \sim U_{0H} + 2\pi \sum_{j=1}^{N} \nu_j \gamma_j G_0(\mathbf{x}; \mathbf{x}_j) + \chi\,, \tag{4.2a}$$

where the γ_j for $j = 1, \ldots, N$ and the constant χ are the solution to the $N+1$ dimensional linear algebraic system

$$\gamma_j \left(\nu_j R_0(\mathbf{x}_j) - 1\right) + 2\pi \sum_{k=1, k\neq j}^{N} \nu_k \gamma_k G_0(\mathbf{x}_j; \mathbf{x}_k) + \chi = -U_{0H}(\mathbf{x}_j)\,, \quad j = 1, \ldots, N\,; \qquad 2\pi \sum_{k=1}^{N} \nu_k \gamma_k = \int_{\Omega} \frac{1}{D(\mathbf{x})}\, d\mathbf{x}\,. \tag{4.2b}$$

Here $\nu_j = -1/\log(\varepsilon d_j)$, d_j is the logarithmic capacitance associated with the j-th prey patch Ω_j, while G_0 is the Neumann Green's function with regular part R_0 satisfying (2.17). In (4.2a), $U_{0H}(\boldsymbol{x})$ is the unique solution to

$$\Delta U_{0H} = -\frac{1}{D(\mathbf{x})} + \frac{1}{|\Omega|} \int_{\Omega} \frac{1}{D(\mathbf{x})}\, d\mathbf{x}\,, \quad \mathbf{x} \in \Omega\,; \qquad \frac{\partial U_{0H}}{\partial n} = 0\,, \quad \mathbf{x} \in \partial\Omega\,; \qquad \int_{\Omega} U_{0H}\, d\mathbf{x} = 0\,. \tag{4.3}$$

In terms of this solution, the average MFPT given a uniform distribution of starting points in Ω is simply χ.

4.1 Numerical Verification

Next, we compare results from our asymptotic theory with full numerical results obtained by solving the MFPT PDE with variable diffusivity using FlexPDE6 [16]. In our computations we took a circular domain of radius 1km, so that the Neumann Green's function is explicitly available. The prey patches are all circles of radius 0.0067km, so that $\varepsilon = 0.0067$.

For simplicity, in order to be able to solve the problem for U_{0H} analytically, we consider two specific forms for $D(\mathbf{x})$. Our first choice is the monotonically decreasing radially symmetric diffusivity

$$D(\mathbf{x}) = \frac{1}{1+|\mathbf{x}|^2}\,. \tag{4.4}$$

For this choice, the solution U_{0H} to (4.3) is radially symmetric and is readily calculated as

$$U_{0H} = \frac{r^2}{8} - \frac{r^4}{16} - \frac{1}{24}\,. \tag{4.5}$$

Our second choice for variable diffusivity is

$$D = \frac{1}{a_0 + a_1\cos^2(2\theta)}\,, \tag{4.6}$$

for $a_0 > 0$ and $a_1 > 0$, chosen so that the $D_{\rm ave} \equiv \pi^{-1}\int_\Omega D(\mathbf{x})\,d\mathbf{x} = 1$ is unity. Since $\int_0^{2\pi}\left[a_0 + a_1\cos^2\omega\right]^{-1}\,d\omega = 2\pi\left[\sqrt{a_0}\sqrt{a_1+a_0}\right]^{-1}$ from residue calculus, then $D_{\rm ave} = 1$ when $a_0(a_1+a_0) = 1$. With this choice, we can contrast the effect of variable diffusivity with that of a spatially uniform diffusivity with $D = 1$. For D as given in (4.6), the problem (4.3) reduces to $\Delta u_{0H} = -(a_1/2)\cos(4\theta)$. By separating variables, the solution to (4.3) is

$$U_{0H} = \frac{a_1}{24}\left(r^2 - \frac{r^4}{2}\right)\cos(4\theta)\,. \tag{4.7}$$

Below, the results from the asymptotic theory and those computed from the full PDE (4.1) are given in terms of the average MFPT, which assumes a uniform distribution of starting points in the unit disk. Assuming $D_{\rm dim} = 0.41{\rm km}^2/{\rm hr}$ and $L = 1{\rm km}$ as the radius of the circular landscape Ω, the dimensional asymptotic and numerical results are

$$T_{\rm asy} \equiv \chi/0.41\,, \qquad T_{\rm num} \equiv \frac{1}{0.41|\Omega\backslash\Omega_p|}\int_{\Omega\backslash\Omega_p} u(\mathbf{x})\,d\mathbf{x}\,, \tag{4.8}$$

where Ω is the unit disk, Ω_p is the union of all the prey patches, u solves (4.1), and χ is calculated from (4.2).

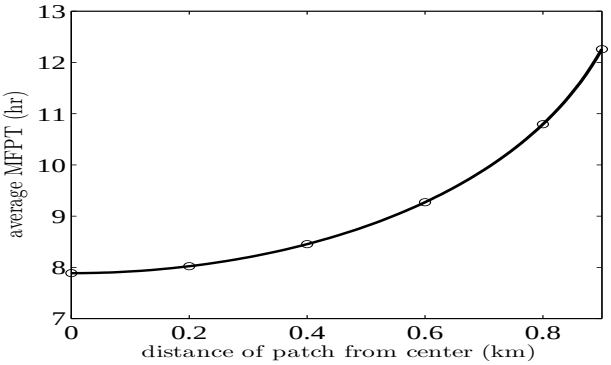

Fig. 8 For a single circular patch of radius $\varepsilon = 0.0067$ centered at a distance r_0 from the origin in the unit disk Ω for the variable diffusivity (4.1), the asymptotic (solid curve) and full numerical results (open circles), as defined in (4.8), for the dimensional average MFPT are compared for a range of r_0.

We first consider the radially symmetric diffusivity (4.4) with a single circular patch of radius $\varepsilon = 0.0067$ centered at a distance r_0 from the origin in Ω. In Fig. 8 we show a very favorable comparison between the asymptotic and numerical results for the average MFPT as r_0 varies on $0 < r_0 < 1$. As expected, from the monotone decreasing behavior of $D = D(|\mathbf{x}|)$, the value of the average MFPT increases with the distance r_0 of the patch from the center.

Next, for the diffusivity (4.4), in Table 4 we show a very close comparison between the asymptotic and numerical results for the average MFPT when the unit disk contains three circular patches of radius $\varepsilon = 0.0067$. The results in Table 4 are shown for the same patch configurations considered in Table 2 for the case $D \equiv 1$ with no drift.

Patch1	Patch2	Patch3	avg. MFPT (hr) (asy)	avg. MFPT (hr) (num)
(0.5,0.3)	(-0.2,0.6)	(-0.4,-0.7)	2.5283	2.5283
(0.3,0.8)	(0.1,-0.6)	(-0.5,-0.7)	2.9679	2.9678

Table 4 Asymptotic and numerical results for the average MFPT are compared for two different three-patch configurations in the unit disk. Each circular patch has radius $\varepsilon = 0.0067$ and the variable diffusivity is given in (4.4).

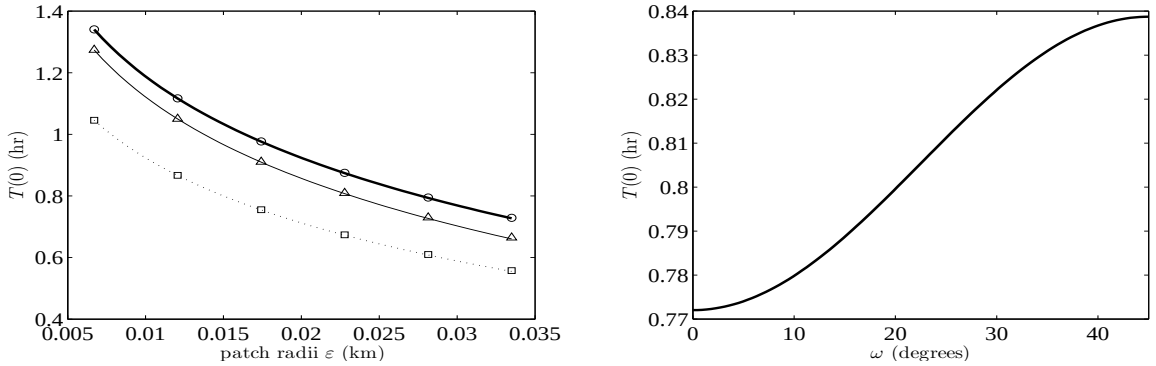

Fig. 9 Left panel: Asymptotic results from Principal Result 4.1 (solid curves) and full numerical results computed from the PDE (4.1) (discrete points) for the dimensional MFPT $T(0)$ versus the patch radius ε for two different four circular patch patterns under the diffusivity model (4.6) with $a_0 = 1/2$ and $a_1 = 3/2$ for which $|\Omega|^{-1}\int_\Omega D\,d\mathbf{x} = 1$. The heavy solid curve is for patches centered at $(\pm 0.5/\sqrt{2}, \pm 0.5/\sqrt{2})$, which lie along the rays where D is maximized. The solid curve is for patches centered at $(\pm 0.5, 0)$ and $(0, \pm 0.5)$, which lie along the rays where D is minimized. For comparison, the dotted curve corresponds to a spatially uniform diffusivity $D \equiv 1$ for which $|\Omega|^{-1}\int_\Omega D\,d\mathbf{x} = 1$. Right panel: Asymptotic results for $T(0)$ for four circular patches of radius $\varepsilon = 0.025$ centered at $\mathbf{x}_j = 0.5\,(\cos(\omega + \pi j/2), \sin(\omega + \pi j/2))$, for $j = 0, \ldots, 3$, where $0 \le \omega \le \pi/4$. When $\omega = 0$ and $\omega = \pi/4$ the traps are aligned with the rays of minimum and maximum diffusivity, respectively. We observe that $\omega = 0$ minimizes $T(0)$.

Finally, we consider the diffusivity model (4.6) with $a_0 = 1/2$ and $a_1 = 3/2$ for which $|\Omega|^{-1}\int_\Omega D\,d\mathbf{x} = 1$. For this model, D achieves its maximum value on the rays $\theta = \pm\pi/4$ and $\theta = \pm 3\pi/4$, and its minimum value on the rays $\theta = \pm\pi/2$ and $\theta = 0, \pi$. In the left panel of Fig. 9, we consider two different patterns consisting of four circular patches, each of radius ε, that are placed equidistantly on a concentric ring of radius 0.5 in the unit disk. The first pattern has patches centered at $(\pm 0.5/\sqrt{2}, \pm 0.5/\sqrt{2})$, which lie along the rays where D is maximized. In contrast, the second pattern has patches centered at $(\pm 0.5, 0)$ and $(0, \pm 0.5)$, which lie along the rays where D is minimized. For both patterns, in the left panel of Fig. 9 we compare asymptotic and full numerical values for the MFPT as a function of ε on $0.0067 < \varepsilon < 0.0335$, when the starting point is at the center of the disk. The asymptotic result, measured in hours, is $T(0) = u(0)/(0.41)$, where $u(0)$ is computed from (4.2a) of Principal Result 4.1. The corresponding full numerical result is computed from the PDE (4.1). For comparison, in the left panel of Fig. 9 we also plot the corresponding result assuming a spatially uniform diffusivity with $D = 1$ for which $|\Omega|^{-1}\int_\Omega D\,d\mathbf{x} = 1$.

From the left panel of Fig. 9, we conclude that the effect of a variable diffusivity is to increase the MFPT $T(0)$. Moreover, we observe, somewhat counter-intuitively, that the MFPT $T(0)$ is larger when the patches are aligned with the rays upon which D is maximized. A possible explanation for this result is that the MFPT to a patch occurs as a result of Brownian motion through all paths that begin at the origin, thereby sampling regions of the landscape where D is both large and small. The MFPT $T(0)$ does not occur simply from a directed, or funneled, motion from the origin along a ray where D is maximized. In fact, our results suggest that the expected capture time is smaller when the patch is located near where D is smaller, suggesting that the predator catches its prey faster when it diffuses more slowly near the patch. To further examine the issue regarding the orientation of the patches with respect to the rays upon which D is maximized, we next center the four traps at $\mathbf{x}_j = 0.5\,(\cos(\omega + \pi j/2), \sin(\omega + \pi j/2))$ for $j = 0, \ldots, 3$, where $0 \le \omega \le \pi/4$. When $\omega = 0$ and $\omega = \pi/4$ the traps are aligned with the rays of minimum and maximum diffusivity, respectively. In the right panel of Fig. 9 we plot the asymptotic result for $T(0)$ versus this alignment angle ω for fixed $\varepsilon = 0.025$. This plot shows that the two solid curves in the left panel of Fig. 9, corresponding to patch alignment with the rays of minimum and maximum diffusivity, do provide the minimum and maximum values of $T(0)$, respectively.

5 Asymptotic Calculation of the Splitting Probability

In this section we use the hybrid asymptotic-numerical method for summing logarithmic expansions to calculate a splitting probability. Here we assume that the predator diffuses randomly on a landscape with N possible prey patches. One of the prey patches, referred to as the target patch, is preferable to the predator. Our goal is to calculate the splitting probability, defined as the probability of reaching this target patch before any of the other $N-1$ possible patches.

The probability, $u(\mathbf{x})$ of reaching a specific target patch before any of the other patches satisfies (cf. [41]):

$$\begin{aligned} \Delta u(\mathbf{x}) = 0\,, \quad \mathbf{x} \in \Omega \setminus \cup_{j=1}^{N} \Omega_j^\varepsilon\,; \qquad \frac{\partial u}{\partial n} = 0\,, \quad \mathbf{x} \in \partial\Omega\,, \\ u = \delta_{1j}\,, \quad \mathbf{x} \in \partial\Omega_j^\varepsilon\,, \quad j = 1, \ldots, N\,, \end{aligned} \tag{5.1}$$

where δ_{1j} is the Kronecker symbol, with $\delta_{1j} = 1$ if $j = 1$ and $\delta_{1j} = 0$ otherwise. In (5.1) the target patch as Ω_1^ε. We again assume that as $\varepsilon \to 0$, $\Omega_j^\varepsilon \to \mathbf{x}_j \in \Omega$ for $j = 1 \ldots, N$, and that $|\mathbf{x}_i - \mathbf{x}_j| = \mathcal{O}(1)$ for $i \neq j$.

5.1 Asymptotic Analysis

In the outer region, away from the patches, we expand the solution to (5.1) as

$$u \sim U_0(\mathbf{x}, \boldsymbol{\nu}) + \sigma(\varepsilon) U_1(\mathbf{x}, \boldsymbol{\nu}) + \ldots\,. \tag{5.2}$$

Here $\boldsymbol{\nu} \equiv (\nu_1, \ldots, \nu_N)$ with $\nu_j = -1/\log \varepsilon d_j$, where the logarithmic capacitance d_j is defined by (2.6). As before, the gauge function σ is beyond-all-orders with respect to the logarithmic gauge terms.

Upon substituting the expansion (5.2) into (5.1) we obtain that the outer solution U_0 satisfies

$$\Delta U_0 = 0\,, \quad \mathbf{x} \in \Omega \setminus \{\mathbf{x}_1, \ldots, \mathbf{x}_N\}\,; \qquad \frac{\partial U_0}{\partial n} = 0\,, \quad \mathbf{x} \in \partial\Omega\,. \tag{5.3}$$

Since, in the outer region, the patches shrink to the points $\mathbf{x}_j \in \Omega$ as $\varepsilon \to 0$ for $j = 1, \ldots, N$, this problem must be supplemented by appropriate singularity conditions as $\mathbf{x} \to \mathbf{x}_j$ for each $j = 1, \ldots, N$.

For the inner problem near the j-th patch, we define $\mathbf{y} \equiv \varepsilon^{-1}(\mathbf{x} - \mathbf{x}_j)$, and the magnified inner domain $\Omega_j \equiv \varepsilon^{-1}\Omega_j^\varepsilon$. In terms of $\mathbf{y}$, we define the inner solution $q_j(\mathbf{y})$ as $q_j(\mathbf{y}) = u(\mathbf{x}_j + \varepsilon\mathbf{y})$, and we expand it as

$$q_j \sim \delta_{1j} + \nu_j \gamma_j(\boldsymbol{\nu}) q_{0j}(\mathbf{y}) + \alpha(\varepsilon, \boldsymbol{\nu}) q_{1j}(\mathbf{y}) + \ldots\,, \tag{5.4}$$

where γ_j is an unknown constant to be determined and α is transcendentally small with respect to any power of ν_j. Upon substituting (5.4) into (5.1), we obtain that q_{0j} satisfies (2.6).

Next, by using the far-field behavior of q_{0j} as $|\mathbf{y}| \to \infty$ from (2.6), we obtain from the matching condition between the inner and outer solution that U_0 must have the singularity behavior

$$U_0 \sim \delta_{1j} + \nu_j \gamma_j \log|\mathbf{x} - \mathbf{x}_j| + \gamma_j\,, \quad \text{as} \quad \mathbf{x} \to \mathbf{x}_j\,, \tag{5.5}$$

for each $j = 1, \ldots, N$. The problem for the outer solution is then (5.3) subject to the singularity behaviors (5.5) for each $j = 1, \ldots, N$. These conditions lead to a linear algebraic system for γ_j for $j = 1, \ldots, N$.

The problem (5.3) subject to (5.5) can be written in Ω in terms of Dirac delta functions as

$$\Delta U_0 = 2\pi \sum_{k=1}^{N} \nu_k \gamma_k \delta(\mathbf{x} - \mathbf{x}_k)\,, \quad \mathbf{x} \in \Omega\,; \qquad \frac{\partial U_0}{\partial n} = 0\,, \quad \mathbf{x} \in \partial\Omega\,, \tag{5.6}$$

subject to (5.5). By applying the divergence theorem to (5.6), we obtain the constraint that

$$2\pi \sum_{k=1}^{N} \nu_k \gamma_k = 0\,. \tag{5.7}$$

We then write the solution to (5.6) as

$$U_0 = 2\pi \sum_{k=1}^{N} \nu_k \gamma_k G_0(\mathbf{x}; \mathbf{x}_k) + \chi\,, \qquad \chi \equiv \frac{1}{|\Omega|} \int_\Omega U_0(\mathbf{x})\, d\mathbf{x}\,, \tag{5.8}$$

where χ is to be found and $G_0(\mathbf{x};\boldsymbol{\xi})$ is the Neumann Green's function satisfying (2.17).

To determine the linear algebraic system for γ_j for $j = 1,\dots,N$ and χ we expand (5.8) as $\mathbf{x} \to \mathbf{x}_j$, and enforce the required singular behavior (5.5). This leads, for each $j = 1,\dots,N$, to

$$2\pi \sum_{k=1,k\neq j}^{N} \nu_k\gamma_k G_0(\mathbf{x}_k;\mathbf{x}_j) + \nu_j\gamma_j(\log|\mathbf{x}-\mathbf{x}_j| + R_0(\mathbf{x}_j)) + \chi \sim \delta_{1j} + \nu_j\gamma_j \log|\mathbf{x}-\mathbf{x}_j| + \gamma_j\,.$$

The singular terms match identically, while the non-singular terms provide the linear algebraic system for the γ_j for $j = 1,\dots,N$ and χ. We summarize our result as follows.

Principal Result 5.1: *For $\varepsilon \to 0$, the asymptotic solution for the splitting probability (5.1) is given in the outer region $|\boldsymbol{x}-\boldsymbol{x}_j| \gg \mathcal{O}(\varepsilon)$ for $j = 1,\dots,N$ by*

$$u \sim 2\pi \sum_{k=1}^{N} \nu_k\gamma_k G_0(\mathbf{x};\mathbf{x}_k) + \chi\,, \tag{5.9}$$

where γ_j for $j = 1,\dots,N$ and χ are to be determined from the $N+1$ dimensional linear algebraic system

$$\gamma_j\,(\nu_j R_0(\mathbf{x}_j) - 1) + 2\pi \sum_{k=1,k\neq j}^{N} \nu_k\gamma_k G_0(\mathbf{x}_j;\mathbf{x}_k) + \chi = \delta_{1j}\,, \quad j = 1,\dots,N\,; \qquad \sum_{k=1}^{N} \nu_k\gamma_k = 0\,. \tag{5.10}$$

This linear system is solvable when $\nu_{max} \equiv \max_j \nu_j$ is sufficiently small.

5.2 Numerical Verification

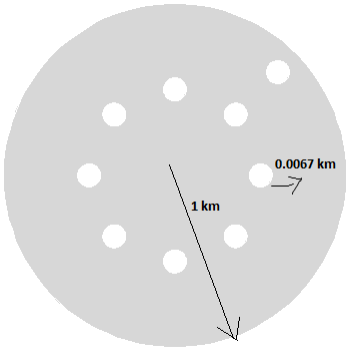

Fig. 10 Model domain for numerical experiments. Non-target patches are located on a concentric ring within a circular-shaped landscape Ω with the target patch located outside the ring.

We now verify Principal Result 5.1 of our asymptotic analysis with full numerical results computed from (5.1) using FlexPDE6 [16]. In each of the numerical experiments below, Ω is a circular domain of radius 1km, for which the Neumann Green's function and its regular part are known from (2.17). Most of our results are quoted in terms of the average splitting probability, defined as $u_{\text{ave}} = |\Omega|^{-1}\int_\Omega u\,d\mathbf{x}$. The asymptotic result for this average probability is χ from (5.10).

We focus on the scenario where there are either four or eight non-target circular patches of radius ε that are equally spaced on a concentric ring inside the circular domain Ω. The circular target patch, also of radius ε, is located either outside or inside the ring. The case of eight patches on a ring is shown schematically in Fig. 10.

For our first experiment we put four patches on a ring of radius 0.5 centered at $(0.3, 0.4)$, $(-0.3, 0.4)$, $(0.3, -0.4)$, and $(-0.3, -0.4)$. For two locations of the target patch, and for $\varepsilon = 0.0067$, in Table 5 we show a very favorable agreement between the asymptotic result of Principal Result 5.1 and the full numerical result computed from (5.1).

For our next experiment, we put eight patches on a ring of radius 0.5 centered at $(\pm\frac{1}{2\sqrt{2}}, \pm\frac{1}{2\sqrt{2}})$, $(\pm 0.5, 0)$, and $(0, \pm 0.5)$. The very close agreement between the asymptotic and full numerical results for this case is shown in Table 6.

Target patch location	Asymptotic	Numerical
(0,0.001)	0.17201	0.172019
(0.5,0.5)	0.15899	0.158992

Table 5 Spatial averages of the splitting probability when the circular target is located either inside or outside a four-patch ring with circular patches centered at $(\pm 0.3, \pm 0.4)$. All patches have radius $\varepsilon = 0.0067$. The asymptotic result is χ from (5.10).

Target patch location	Asymptotic	Numerical
(0.001,0)	0.08802	0.08804
(0.65,0.65)	0.08373	0.08374

Table 6 Spatial averages of the splitting probability when the circular target is located either inside or outside an eight-patch ring with circular patches centered at $(\pm\frac{1}{2\sqrt{2}}, \pm\frac{1}{2\sqrt{2}})$, $(\pm 0.5, 0)$, and $(0, \pm 0.5)$. All patches have radius $\varepsilon = 0.0067$. The asymptotic result is χ from (5.10).

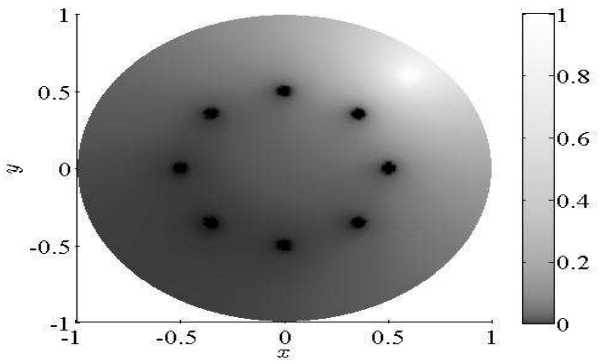

Fig. 11 Full numerical results for the splitting probability computed from (5.1) when the circular target is centered at $(0.6, 0.6)$ outside a ring of eight circular patches centered at $(\pm\frac{1}{2\sqrt{2}}, \pm\frac{1}{2\sqrt{2}})$, $(\pm 0.5, 0)$, and $(0, \pm 0.5)$. The radius of each patch is $5\varepsilon = 0.0335$ where $\varepsilon = 0.0067$.

For this same configuration of eight non-target circular patches equally-spaced on an annular ring with an additional circular target patch, we increase the radius of each patch to $5\varepsilon = 0.0335$. The asymptotic and full numerical results are shown in Table 7 for a target patch that is either inside or outside the ring of patches. For this larger common patch radius, the asymptotic results still agree rather well with the full numerical results. In Fig. 11 we show full numerical results for the splitting probability when the target patch is located outside the ring of patches. From this figure we observe that the probability of reaching the target patch first from an initial starting point that is inside the ring of patches is considerably lower than the fractional ratio $1/N$, where $N = 9$ is the total number of patches. This reduction in the splitting probability from its leading order limiting value of $1/N$ is due to a shielding effect induced by the non-target patches.

Target patch location	Asymptotic	Numerical
(0,0.001)	0.07304	0.07423
(0.6,0.6)	0.08726	0.08695

Table 7 Same caption as in Table 6 except that the radius of each circular patch is increased to $5\varepsilon = 0.0335$.

To further illustrate this shielding effect, we consider our eight-patch configuration with a target patch centered inside the ring at $(0, 0.1)$. The radius of each patch is $\varepsilon = 0.0067$ as in Table 6. In Fig. 12, we plot the splitting probability $u(x, 0)$ along the horizontal axis on the range $-1 < x < 1$. From this figure, we observe that the probability of reaching the target first is largest when the predator starts close to the target patch centered near the origin. However, when the predator starts from an initial location outside the "protective" annular ring, the probability of first reaching the target patch before any of the other patches is significantly lower than $1/N$ where $N = 9$ is the total number of patches. This example shows clearly that the spatial distribution of non-target patches can have a significant influence on the probability of reaching a specific target first.

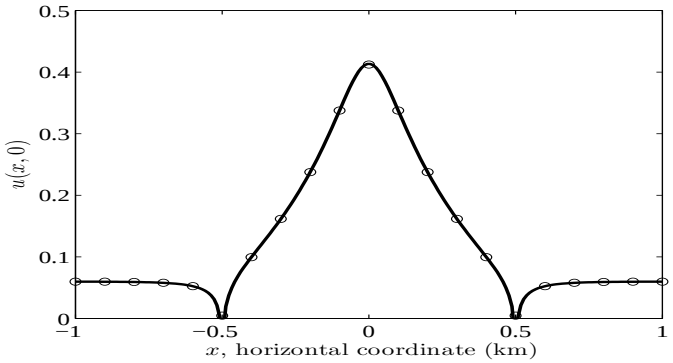

Fig. 12 Comparison of the full numerical results computed from (5.1) (open circles) and the asymptotic results obtained from Principal Result 5.1 (solid curve) for the splitting probability $u(x,0)$ on the horizontal axis, when the circular target is centered at $(0, 0.1)$ inside a ring of eight circular patches centered at $(\pm\frac{1}{2\sqrt{2}}, \pm\frac{1}{2\sqrt{2}})$, $(\pm 0.5, 0)$, and $(0, \pm 0.5)$. The radius of each patch is $\varepsilon = 0.0067$.

5.3 The Effect of Closely Spaced Patches

In our analysis so far, we have assumed that the patches are located at $\mathcal{O}(1)$ distances from each other. We now consider the case where a circular target patch is $\mathcal{O}(\varepsilon)$ close to another circular patch. We assume that these two circular patches do not overlap. These two closely spaced patches can be effectively combined into a two-patch cluster of size $\mathcal{O}(\varepsilon)$ centered at some $\mathbf{x}_1 \in \Omega$. We will assume that there are an additional $N-1$ well-separated patches, not necessarily circular, centered at $\mathbf{x}_j \in \Omega$ for $j = 2, \ldots, N$. For this configuration of patches, the splitting probability satisfies

$$\begin{aligned} &\Delta u(\mathbf{x}) = 0\,, \quad \mathbf{x} \in \Omega \setminus \cup_{j=1}^{N} \Omega_j^\varepsilon\,, \qquad \Omega_1^\varepsilon \equiv \Omega_{1,0}^\varepsilon \cup \Omega_{1,1}^\varepsilon\,; \qquad \frac{\partial u}{\partial n} = 0\,, \quad \mathbf{x} \in \partial\Omega\,, \\ &\quad u = 0\,, \quad \mathbf{x} \in \partial\Omega_j^\varepsilon\,, \quad j = 2, \ldots, N\,, \\ &\quad u = 1\,, \quad \mathbf{x} \in \partial\Omega_{1,0}^\varepsilon\,; \qquad u = 0\,, \quad \mathbf{x} \in \partial\Omega_{1,1}^\varepsilon\,. \end{aligned} \tag{5.11}$$

The key feature for this problem is that we must analyze a new inner problem near the two-patch cluster Ω_1^ε. In this inner region, we introduce the inner variables $\mathbf{y} = \varepsilon^{-1}(\mathbf{x} - \mathbf{x}_1)$ and $q_1(\mathbf{y}) = u(\mathbf{x}_1 + \varepsilon\mathbf{y})$. We then expand q_1 as

$$q_1 \sim q^\star + \nu_1\gamma_1 q_c\,. \tag{5.12}$$

Here $\nu_1 = -1/\log(\varepsilon d_{1c})$, where d_{1c} is the logarithmic capacitance of the two-disk cluster, and $\gamma_1 = \gamma_1(\boldsymbol{\nu})$ is a constant to be determined. In (5.12), the bounded function $q^\star$ is taken to satisfy

$$\begin{aligned} &\Delta_{\mathbf{y}} q^\star = 0\,, \quad \mathbf{y} \notin \Omega_{1,0} \cup \Omega_{1,1}\,, \\ &\quad q^\star = 1\,, \quad \mathbf{y} \in \partial\Omega_{1,0}\,; \qquad q^\star = 0\,, \quad \mathbf{y} \in \partial\Omega_{1,1}\,, \\ &\quad q^\star \sim q_\infty^\star\,, \quad \text{as} \quad |\mathbf{y}| \to \infty\,, \end{aligned} \tag{5.13}$$

where $q_\infty^\star$ is a constant to be determined. Here $\Omega_{1,0} \equiv \varepsilon^{-1}\Omega_{1,0}^\varepsilon$ and $\Omega_{1,1} \equiv \varepsilon^{-1}\Omega_{1,1}^\varepsilon$. In contrast, q_c in (5.12) satisfies

$$\begin{aligned} &\Delta_{\mathbf{y}} q_c = 0\,, \quad \mathbf{y} \notin \Omega_{1,0} \cup \Omega_{1,1}\,, \\ &\quad q_c = 0\,, \quad \mathbf{y} \in \partial\Omega_{1,0}\,; \qquad q_c = 0\,, \quad \mathbf{y} \in \partial\Omega_{1,1}\,, \\ &\quad q_c \sim \log|\mathbf{y}| - \log d_{1c} + o(1)\,, \quad \text{as} \quad |\mathbf{y}| \to \infty\,, \end{aligned} \tag{5.14}$$

where the far-field behavior determines the logarithmic capacitance d_{1c} uniquely.

By using bipolar coordinates, we can solve (5.13) and (5.14) when $\Omega_{1,0}$ and $\Omega_{1,1}$ are two circular disks of radii a_0 and a_1 with a center-to-center separation l, all as measured in the $\mathbf{y}$ variable, with $l > a_0 + a_1$. This allows us to calculate d_{1c} and $q_\infty^\star$ in terms of a_0, a_1, and l. As shown in Appendix A, d_{1c} is given by

$$\log d_{1c} = \log(2c) - \frac{\xi_0\xi_1}{\xi_0 + \xi_1} + \sum_{m=1}^{\infty} \frac{\left[e^{-m\xi_0}\sinh(m\xi_1) + e^{-m\xi_1}\sinh(m\xi_0)\right]}{m\sinh\left[m(\xi_0 + \xi_1)\right]}\,. \tag{5.15}$$

Here $c > 0$ is defined in terms of a_0, a_1, and l by

$$c \equiv \frac{1}{2l}\sqrt{l^2-(a_0+a_1)^2}\sqrt{l^2-(a_0-a_1)^2}\,, \tag{5.16}$$

while $\xi_0 > 0$ and $\xi_1 > 0$ are determined in terms of c, a_0, and a_1 by

$$\xi_0 \equiv \log\left[\frac{c}{a_0}+\sqrt{1+\frac{c^2}{a_0^2}}\right], \qquad \xi_1 \equiv \log\left[\frac{c}{a_1}+\sqrt{1+\frac{c^2}{a_1^2}}\right]. \tag{5.17}$$

Moreover, in Appendix A, we calculate $q_\infty^\star$ from (5.13) in terms of c, a_0, and a_1 as

$$q_\infty^\star = \frac{\xi_1}{\xi_0+\xi_1}\,. \tag{5.18}$$

For circles of a common radius, for which $a_0 = a_1$, (5.18) yields $q_\infty^\star = 1/2$ as expected, and (5.15) reduces to

$$\log d_{1c} = \log(2c) - \frac{\xi_0}{2} + \sum_{m=1}^{\infty}\frac{e^{-m\xi_0}}{m\cosh(m\xi_0)}\,; \qquad c = \sqrt{(l/2)^2-a_0^2}\,, \qquad \xi_0 = \log\left[\frac{l}{2a_0}+\sqrt{\left(\frac{l}{2a_0}\right)^2-1}\right]. \tag{5.19}$$

With the inner solution near the two-patch cluster Ω_1^ε determined in this way, the rest of the analysis for (5.11) proceeds identically as in §5.1. In particular, in the outer region, we expand $u \sim U_0(\mathbf{x};\boldsymbol{\nu}) + \cdots$, to obtain that U_0 satisfies

$$\begin{aligned} &\Delta U_0 = 0\,, \quad \mathbf{x} \in \Omega \setminus \{\mathbf{x}_1,\ldots,\mathbf{x}_N\}\,; \qquad \frac{\partial U_0}{\partial n} = 0\,, \quad \mathbf{x} \in \partial\Omega\,, \\ &U_0 \sim q_\infty^\star \delta_{1,j} + \nu_j\gamma_j \log|\mathbf{x}-\mathbf{x}_j| + \gamma_j\,, \quad \text{as} \quad \mathbf{x} \to \mathbf{x}_j\,, \quad \text{for} \quad j = 1,\ldots,N\,, \end{aligned} \tag{5.20}$$

where $\delta_{1,j}$ is the Kronecker symbol. The unknowns γ_j for $j = 1,\ldots,N$ are determined by solving (5.20) in a similar way as done in §5.1. The result is summarized as follows:

Principal Result 5.2: *For $\varepsilon \to 0$, the asymptotic solution for the splitting probability (5.11) is given in the outer region $|\boldsymbol{x}-\boldsymbol{x}_j| \gg \mathcal{O}(\varepsilon)$ for $j = 1,\ldots,N$ by*

$$u \sim 2\pi\sum_{k=1}^{N}\nu_k\gamma_k G_0(\mathbf{x};\mathbf{x}_k) + \chi\,, \tag{5.21}$$

where γ_j for $j = 1,\ldots,N$ and χ are to be determined from the $N+1$ dimensional linear algebraic system

$$\gamma_j\left(\nu_j R_0(\mathbf{x}_j) - 1\right) + 2\pi\sum_{k=1,k\neq j}^{N}\nu_k\gamma_k G_0(\mathbf{x}_j;\mathbf{x}_k) + \chi = \delta_{1,j}q_\infty^\star\,, \quad j = 1,\ldots,N\,; \qquad \sum_{k=1}^{N}\nu_k\gamma_k = 0\,. \tag{5.22}$$

Here $\nu_1 = -1/\log(\varepsilon d_{1c})$, where d_{1c} is defined in (5.15), $q_\infty^\star$ is defined in (5.18), while $\nu_j = -1/\log(\varepsilon d_j)$ for $j = 2,\ldots,N$, where d_j is determined from (2.6). In (5.22), G_0 is the Neumann Green's function of (2.17) with regular part R_0.

We now compare results from Principal Result 5.2 with corresponding results computed from the full PDE (5.11) for the splitting probability. We first suppose that $N = 1$, so that the two-patch cluster are the only patches in Ω. This models the simple scenario where there are only two patches in Ω, with the circular target patch being $\mathcal{O}(\varepsilon)$ close to another circular patch. Upon setting $N = 1$ in (5.22), we obtain that $\gamma_1 = 0$ and $\chi = q_\infty^\star$. From (5.21), we conclude that the outer solution is spatially uniform and given by $u \sim q_\infty^\star$. This shows, as expected, that the splitting probability is asymptotically independent of the starting point $\mathbf{x} \in \Omega$, when $\mathbf{x}$ is not $\mathcal{O}(\varepsilon)$ close to the two-patch cluster.

From (5.16), (5.17), and (5.18), it can be shown that the outer limit $q_\infty^\star$ depends only on the ratio a_1/a_0 of the disk radii together with the ratio $l/(a_0+a_1)$. To see this, we use (5.16) to calculate the ratios c/a_1 and c/a_0 as

$$\frac{c}{a_1} = \frac{(1+f)}{2fl_0}\sqrt{l_0^2-1}\sqrt{l_0^2-\left(\frac{f-1}{f+1}\right)^2}\,, \qquad \frac{c}{a_0} = f\frac{c}{a_1}\,, \qquad f \equiv \frac{a_1}{a_0}\,, \qquad l_0 \equiv \frac{l}{(a_0+a_1)}\,. \tag{5.23}$$

From (5.17) and (5.18) it follows that $q_\infty^\star$ depends only on f and l_0. Moreover, it is readily confirmed that $0 < q_\infty^\star < 1$. In the left panel of Fig. 13 we plot $q_\infty^\star$ versus a_1/a_0 for various l_0, while in the right panel of Fig. 13 we plot $q_\infty^\star$ versus l_0 for various a_1/a_0.

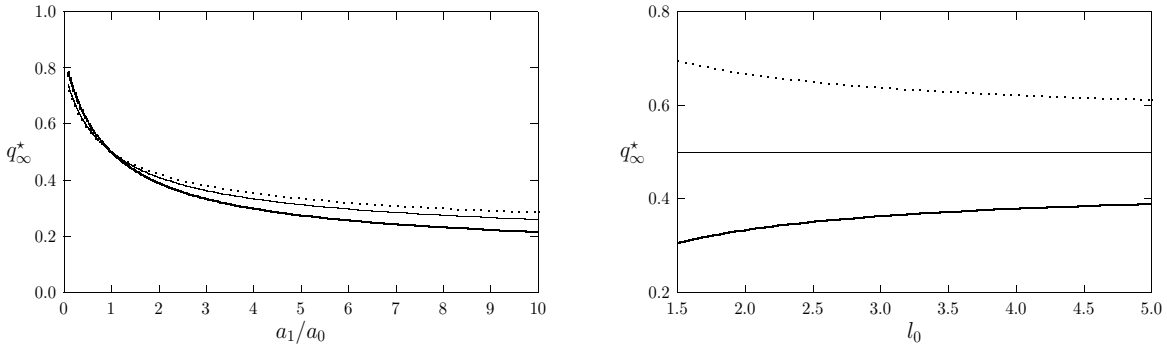

Fig. 13 Left panel: Plot of $q^\star_\infty$ from (5.18) versus a_1/a_0 for $l_0 = 2$ (heavy solid curve), $l_0 = 3$ (solid curve), and $l_0 = 4$ (dotted curve). Here $l_0 = l/(a_1 + a_0)$ where l is the center-to-center separation between the two patches. Right panel: Plot of $q^\star_\infty$ versus l_0 for $a_1/a_0 = 3$ (heavy solid curve), $a_1/a_0 = 1$ (solid curve), and $a_1/a_0 = 1/3$ (dotted curve).

These plots confirm the intuition that when $a_1/a_0 > 1$, so that the target patch has a smaller radius than the other nearby patch, then the fractional probability $q^\star_\infty$ of reaching the target patch first through a Brownian motion starting from any point $\mathbf{x} \in \Omega$ with $\text{dist}(\mathbf{x}, \Omega_1^\varepsilon) = \mathcal{O}(1)$, satisfies $q^\star_\infty < 1/2$. Moreover, these plots show that when both patches have the same radii then, irrespective of the distance between the patches, we have $q^\star_\infty = 1/2$.

To confirm this theoretical prediction, we set $a_1/a_0 = 3$ and $l = 2(a_0 + a_1)$, so that $l_0 = 2$. Then, from (5.18), we calculate explicitly that $q^\star_\infty = 1/3$. To confirm this prediction, we compute full numerical solutions to (5.11) in the unit disk with $N = 1$ with a circular target patch of radius ε centered at the origin and a nearby patch of radius 3ε, centered at $\mathbf{x} = (8\varepsilon, 0)$. Our computations, done for $\varepsilon = 0.0067$, show that $|\Omega|^{-1} \int_{\Omega \setminus \Omega_1^\varepsilon} u \, d\mathbf{x} \approx 0.325$, which is very close to the prediction of $1/3$ from our asymptotic theory.

Next, we consider Principal Result 5.2 for $N = 2$ when Ω is the unit disk. We assume that a circular target patch of radius ε is centered at $(0.25, 0)$ and that there is a nearby circular patch, also of radius ε, which is centered at $(0.25+4\varepsilon, 0)$. Upon setting $a_0 = a_1 = 1$ and $l = 4$ in (5.19) we calculate $d_{1c} = 2.0613$. Furthermore, since $a_0 = a_1$, then $q^\star_\infty = 1/2$ from (5.18). In addition to this two-patch cluster, we assume that there is a further non-target circular patch, also of radius ε, which is centered at $(0, 0.6)$. We choose $\varepsilon = 0.0067$ to be the common radius of the three circular patches. From the linear system (5.22) of Principal Result 5.2 we calculate the asymptotic prediction for the spatial average χ of the splitting probability as $\chi \approx 0.28914$. In contrast, our full numerical results as computed from the PDE (5.11) yields 0.28973 for the spatial average of the splitting probability, which is very close to the asymptotic prediction. The results of the full numerical simulation are shown in Fig. 14.

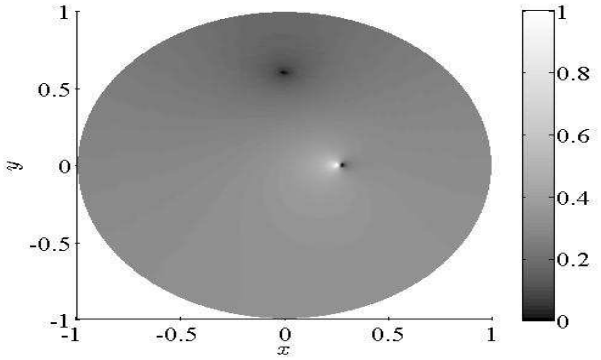

Fig. 14 Full numerical solution for the splitting probability computed from (5.11) for the case of a two-patch cluster centered at $(0.25, 0)$ and $(0.25 + 4\varepsilon, 0)$, with an additional (remote) circular patch centered at $(0, 0.6)$. Each patch has a radius $\varepsilon = 0.0067$. Notice that the probability of first reaching the target patch is only relatively high when starting near the target patch. In addition, due to a shielding effect, this probability is rather low when starting from behind the remote patch at $(0, 0.6)$.

In a similar way, we can modify the formulae in Principal Result 2.1 for the MFPT to analyze the case when two patches are closely spaced by $\mathcal{O}(\varepsilon)$. Suppose that the patches with centers $\mathbf{x}_{N-1}$ and $\mathbf{x}_N$, satisfy $|\mathbf{x}_N - \mathbf{x}_{N-1}| = \mathcal{O}(\varepsilon)$. In this case, the inner problem (5.14) for a two-patch cluster replaces the canonical inner problem (2.6) associated with isolated patches. To use (2.15) in Principal Result 2.1 to calculate the asymptotic MFPT, we can simply replace the locations $\mathbf{x}_N$ and $\mathbf{x}_{N-1}$ with $\mathbf{x}_c \equiv (\mathbf{x}_N + \mathbf{x}_{N-1})/2$ and replace the gauge functions ν_{N-1} and ν_N with $\nu_c \equiv -1/\log(\varepsilon d_{1c})$, where d_{1c} is the logarithmic capacitance of the two-patch cluster, as defined by the far-field behavior in (5.14). Then, (2.15) becomes a linear system for χ and γ_j for $j = 1, \ldots, N-1$ where $\gamma_{N-1} \equiv \gamma_c$ is the strength associated with the two-patch cluster. When the two closely-spaced patches are circular disks, d_{1c} is known analytically from (5.15).

The effectiveness of Principal Result 2.1 for the case of two closely spaced patches is illustrated in Table 8 for three circular traps of a common radius $\varepsilon = 0.025$ and with drift parameter $\beta = 0.085/0.41$. In Table 8 we compare full numerical and asymptotic results for the distributional average of the MFPT for three different spatial configurations of the three circular patches. In our examples, the two circular patches centered on the horizontal axis are become increasingly close together. The asymptotic results in Table 8 are obtained by either treating the closely spaced patches as a "cluster", as described above, or else as "isolated" patches. In calculating the logarithmic capacitance of the cluster we used (5.19). The results show that when two patches are closely spaced, it is preferable to approximate them as a cluster.

Patch1	Patch2	Patch3	min. separ. (km)	avg. MFPT (hr) (num)	isolated (hr) (asy)	cluster (hr) (asy)
(-0.5,0.5)	(0.5,0)	(0.7, 0)	0.15	1.5149	1.5178	1.5101
(-0.5,0.5)	(0.5,0)	(0.6, 0)	0.05	1.5952	1.6067	1.5938
(-0.5,0.5)	(0.5,0)	(0.56, 0)	0.01	1.6600	1.6890	1.6593

Table 8 Full numerical and asymptotic results for the distributional average of the MFPT for three different spatial configurations of three circular patches. The patches have a common radius $\varepsilon = 0.025$ and the drift parameter is $\beta = 0.085/0.41$. The sixth and seventh columns are the asymptotic results when the two closely spaced patches are treated as isolated and as a cluster, respectively. The results show that as the two patches become closer, a better asymptotic approximation to the MFPT is obtained by treating them as a two-patch cluster with a logarithmic capacitance computed from (5.19).

6 Second Moment Analysis and Estimation of Variance

Previously we have developed and implemented a hybrid asymptotic-numerical method to approximate the MFPT for a predator to catch a prey. However, it may also be important to estimate second-moment information, such as the variance, when the first passage time has a significant spread around the mean. In order to determine the variance of the first passage time (VMFPT), we will first calculate the second moment of the first passage time (SMFPT).

It is well-known that the SMFPT satisfies the following PDE in dimensional form (cf. [41]):

$$D\Delta' M(\mathbf{X}) + 2T' = 0\,. \tag{6.1}$$

Here D is the constant diffusivity, T' is the mean first passage time, and M is the second moment of the first passage time. The PDE is made dimensionless by defining $w = \frac{D^2}{L^4} M$ and $\mathbf{x} = L^{-1}\mathbf{X}$. The primed operators are defined with respect to $\mathbf{X}$, while the un-primed ones are with respect to the non-dimensional variable $\mathbf{x}$. In addition, L is the characteristic length of the domain under consideration. Recall that $T = \frac{D}{L^2} T'$, which is the non-dimensionalization used in the analysis of the MFPT in §2. The corresponding PDE for the second moment in non-dimensional variables is

$$\begin{aligned} \Delta w(\mathbf{x}) = -2T\,, \quad \mathbf{x} \in \Omega \setminus \cup_{j=1}^{N} \Omega_j^{\varepsilon}\,; \qquad \frac{\partial w}{\partial n} = 0\,, \quad \mathbf{x} \in \partial\Omega\,, \\ w = 0\,, \quad \mathbf{x} \in \partial\Omega_j^{\varepsilon}\,, \quad j = 1, \ldots, N\,. \end{aligned} \tag{6.2}$$

In (6.2), the asymptotic result for the MFPT T in the outer region was given by (2.16) of Principal Result 2.2.

6.1 Asymptotic Analysis

We now construct the solution to (6.2) asymptotically. The outer expansion has the form

$$w \sim W_0(\mathbf{x}, \boldsymbol{\nu}) + \sigma(\varepsilon) W_1(\mathbf{x}, \nu) + \ldots\,,$$

where $\boldsymbol{\nu} \equiv (\nu_1, \ldots, \nu_N)$ with $\nu_j = -1/\log(\varepsilon d_j)$, and σ is assumed to be beyond-all-orders with respect to the logarithmic gauge terms. The problem for W_0 is

$$\Delta W_0 = -2T\,, \quad \mathbf{x} \in \Omega \setminus \{\mathbf{x}_1, \ldots, \mathbf{x}_N\}\,; \qquad \frac{\partial W_0}{\partial n} = 0\,, \qquad \mathbf{x} \in \partial\Omega\,, \tag{6.3}$$

subject to certain singularity conditions as $\mathbf{x} \to \mathbf{x}_j$ for $j = 1, \ldots, N$. Up to negligible $\mathcal{O}(\varepsilon)$ terms, the inner problem near the j-th patch is identical to the one obtained in (2.6) for the MFPT without drift. By using the far-field behaviour of the inner solution from (2.6), we match the inner and outer solutions to derive that W_0 must satisfy

$$W_0 \sim \nu_j \gamma_j \log|\mathbf{x} - \mathbf{x}_j| + \gamma_j\,, \quad \text{as} \quad \mathbf{x} \to \mathbf{x}_j\,, \quad j = 1, \ldots, N\,, \tag{6.4}$$

where $\gamma_j = \gamma_j(\boldsymbol{\nu})$ is a constant to be determined. Here $\nu_j = -1/\log(\varepsilon d_j)$ and d_j is the logarithmic capacitance of the j-th patch Ω_j, as defined by the canonical inner problem (2.6).

Next, by incorporating the correct strength of the logarithmic singularity, (6.3) can be written in Ω as

$$\Delta W_0 = -2T + 2\pi \sum_{k=1}^{N} \nu_k \gamma_k \delta(\mathbf{x} - \mathbf{x}_k)\,, \quad \mathbf{x} \in \Omega\,; \qquad \frac{\partial W_0}{\partial n} = 0\,, \quad \mathbf{x} \in \partial\Omega\,, \tag{6.5}$$

subject to the singularity behaviors (6.4). From the MFPT result (2.16) of Principal Result 2.2, in the outer region T has the outer asymptotic expansion

$$T \sim 2\pi \sum_{k=1}^{N} \nu_k \Gamma_k G_0(\mathbf{x}; \mathbf{x}_k) + \chi\,, \tag{6.6}$$

where $\Gamma_k = \Gamma_k(\boldsymbol{\nu})$ for $k = 1, \ldots, N$ and χ satisfy the $N+1$ dimensional linear algebraic system

$$\Gamma_j\,(\nu_j R_0(\mathbf{x}_j) - 1) + 2\pi \sum_{k=1, k\neq j}^{N} \nu_k \Gamma_k G_0(\mathbf{x}_j; \mathbf{x}_k) + \chi = 0\,, \quad j = 1, \ldots, N\,; \qquad 2\pi \sum_{j=1}^{N} \nu_j \Gamma_j = |\Omega|\,. \tag{6.7}$$

Here G_0 is the Neumann Green's function with regular part R_0, defined by (2.17). By substituting (6.6) into (6.5), we obtain that

$$\begin{aligned} &\Delta W_0 = -4\pi \sum_{k=1}^{N} \nu_k \Gamma_k G_0(\mathbf{x}; \mathbf{x}_k) - 2\chi + 2\pi \sum_{k=1}^{N} \nu_k \gamma_k \delta(\mathbf{x} - \mathbf{x}_k)\,, \quad \mathbf{x} \in \Omega\,; \qquad \frac{\partial W_0}{\partial n} = 0\,, \quad \mathbf{x} \in \partial\Omega\,, \\ &W_0 \sim \nu_j \gamma_j \log|\mathbf{x} - \mathbf{x}_j| + \gamma_j\,, \quad \text{as} \quad \mathbf{x} \to \mathbf{x}_j\,, \quad j = 1, \ldots, N\,. \end{aligned} \tag{6.8}$$

To determine a constraint on the unknowns γ_j for $j = 1, \ldots, N$, we integrate (6.8) and use $\int_\Omega G_0(\mathbf{x}; \mathbf{x}_k)\, d\mathbf{x} = 0$ together with the divergence theorem to get

$$\sum_{k=1}^{N} \nu_k \gamma_k = \frac{\chi |\Omega|}{\pi}\,. \tag{6.9}$$

We then decompose the solution to (6.8) as

$$W_0 = W_{0H} + W_{0p}\,, \qquad W_{0p} \equiv -4\pi \sum_{k=1}^{N} \nu_k \Gamma_k W_{0pk}\,, \tag{6.10}$$

where $W_{0pk} = W_{0pk}(\mathbf{x})$ for each $k = 1, \ldots, N$, satisfies

$$\Delta W_{0pk} = G_0(\mathbf{x}; \mathbf{x}_k)\,, \quad \mathbf{x} \in \Omega\,; \qquad \frac{\partial W_{0pk}}{\partial n} = 0\,, \quad \mathbf{x} \in \partial\Omega\,; \qquad \int_\Omega W_{0pk}\, d\mathbf{x} = 0\,. \tag{6.11}$$

In contrast, the other term, W_{0H}, in the decomposition (6.10) satisfies

$$\begin{aligned} &\Delta W_{0H} = -2\chi + 2\pi \sum_{k=1}^{N} \nu_k \gamma_k \delta(\mathbf{x} - \mathbf{x}_k)\,, \quad \mathbf{x} \in \Omega\,; \qquad \frac{\partial W_{0H}}{\partial n} = 0\,, \quad \mathbf{x} \in \partial\Omega\,, \\ &W_{0H} \sim -W_{0p}(\mathbf{x}_j) + \nu_j \gamma_j \log|\mathbf{x} - \mathbf{x}_j| + \gamma_j\,, \quad \text{as} \quad \mathbf{x} \to \mathbf{x}_j\,, \quad j = 1 \ldots, N\,. \end{aligned} \tag{6.12}$$

The solution to (6.12) can be written as $W_{0H} = 2\pi \sum_{k=1}^{N} \nu_k \gamma_k G_0(\mathbf{x};\mathbf{x}_k) + \chi_{0H}$, where χ_{0H} is a constant to be determined. Since $\int_\Omega W_{0p}(\mathbf{x})\,d\mathbf{x} = 0$, this constant can be interpreted as the spatial average $\chi_{0H} = |\Omega|^{-1}\int_\Omega W_0(\mathbf{x})\,d\mathbf{x}$.

Finally, we expand W_{0H} as $\mathbf{x} \to \mathbf{x}_j$ and compare the resulting expression with the required singularity behavior in (6.12). This yields for each $j = 1, \ldots, N$ that

$$2\pi \sum_{k=1,k\neq j}^{N} \nu_k\gamma_k G_0(\mathbf{x}_j;\mathbf{x}_k) + \nu_j\gamma_j\left(\log|\mathbf{x}-\mathbf{x}_j| + R_0(\mathbf{x}_j)\right) + \chi_{0H} \sim \nu_j\gamma_j \log|\mathbf{x}-\mathbf{x}_j| + \gamma_j - W_{0p}(\mathbf{x}_j)\,.$$

The logarithmic terms agree automatically, and from the remaining terms we obtain a linear algebraic system for γ_j for $j = 1, \ldots, N$ and for χ_{0H}. We summarize the result as follows:

Principal Result 6.1: *For $\varepsilon \to 0$, the asymptotic solution for the second moment (6.2) is given in the outer region $|\boldsymbol{x} - \boldsymbol{x}_j| \gg \mathcal{O}(\varepsilon)$ for $j = 1, \ldots, N$ by*

$$w \sim 2\pi \sum_{j=1}^{N} \nu_j\gamma_j G_0(\mathbf{x};\mathbf{x}_j) + W_{0p}(\mathbf{x}) + \chi_{0H}\,, \qquad W_{0p}(\mathbf{x}) = -4\pi \sum_{j=1}^{N} \nu_j \Gamma_j W_{0pj}(\mathbf{x})\,, \tag{6.13a}$$

where Γ_j for $j = 1, \ldots, N$ satisfy (6.7) and W_{0pj} satisfies (6.11). In (6.13a), γ_j for $j = 1, \ldots, N$ and χ_{0H} are determined from the $N + 1$ dimensional linear algebraic system

$$\gamma_j\left(\nu_j R_0(\mathbf{x}_j) - 1\right) + 2\pi \sum_{k=1,k\neq j}^{N} \nu_k\gamma_k G_0(\mathbf{x}_j;\mathbf{x}_k) + \chi_{0H} = -W_{0p}(\mathbf{x}_j)\,; \qquad \sum_{k=1}^{N} \nu_k\gamma_k = \frac{\chi|\Omega|}{\pi}\,, \tag{6.13b}$$

where χ is determined from the linear algebraic system (6.7).

To solve (6.13b), we must calculate $W_{0p}(\mathbf{x}_j)$ for $j = 1, \ldots, N$, where W_{0p} is defined in (6.13a) in terms of the solution W_{0pk} to (6.11). To determine $W_{0pk}(\mathbf{x}_j)$ we apply Green's identity to (6.11) and the problem (2.17) for $G_0(\mathbf{x};\mathbf{x}_j)$ to derive

$$0 = \int_\Omega \left(W_{0pk}\Delta G_0(\mathbf{x};\mathbf{x}_j) - G_0(\mathbf{x};\mathbf{x}_j)\Delta W_{0pk}\right)\,d\mathbf{x} = \int_\Omega \left(W_{0pk}\left[-\frac{1}{|\Omega|} + \delta(x-x_j)\right] - G_0(\mathbf{x};\mathbf{x}_j)G_0(\mathbf{x};\mathbf{x}_k)\right)\,d\mathbf{x}\,.$$

Since $\int_\Omega W_{0pk}\,d\mathbf{x} = 0$ from (6.11), we get that $W_{0pk}(\mathbf{x}_j) = \int_\Omega G(\mathbf{x};\mathbf{x}_j)G(\mathbf{x};\mathbf{x}_k)\,d\mathbf{x}$. This determines $W_{0p}(\mathbf{x}_j)$ in (6.13a) as

$$W_{0p}(\mathbf{x}_j) = -4\pi \sum_{k=1}^{N} \nu_k\Gamma_k\left(\int_\Omega G_0(\mathbf{x};\mathbf{x}_j)G_0(\mathbf{x};\mathbf{x}_k)\,d\mathbf{x}\right)\,. \tag{6.14}$$

In the next subsection, we solve the linear system (6.13b) for χ_{0H} when Ω is the unit disk. For this case, the Neumann Green's function and its regular part are given explicitly in (2.18). For a given patch configuration the two-dimensional integrals in (6.14) over the unit disk are calculated numerically using the cubature Gaussian quadrature rules of [48].

6.2 Numerical Verification

We now confirm the results of the asymptotic analysis with full numerical solutions of the PDE (6.2) computed using FlexPDE6 [16] when Ω is the unit disk. To determine the SMFPT numerically we solve the coupled PDE system for the MFPT and SMFPT given by

$$\begin{aligned} &\Delta w(\mathbf{x}) = -2T\,, \qquad \Delta T(\mathbf{x}) = -1\,, \quad \mathbf{x} \in \Omega \setminus \cup_{j=1}^{N}\Omega_j^\varepsilon\,; \qquad \frac{\partial w}{\partial n} = 0\,, \quad \frac{\partial T}{\partial n} = 0\,, \quad \mathbf{x} \in \partial\Omega\,, \\ &\qquad w = 0\,, \quad T = 0\,, \quad \mathbf{x} \in \partial\Omega_j^\varepsilon\,, \quad j = 1, \ldots, N\,. \end{aligned} \tag{6.15}$$

In terms of the non-dimensional SMFPT w from (6.15), the dimensional SMFPT M is obtained from $M = wL^4/D_{\rm dim}^2$, where $L = 1$km is the radius of Ω and $D_{\rm dim} = 0.41\text{km}^2/\text{hr}$. In our numerical experiments below we consider circular prey patches of a common radius $\varepsilon = 0.0067$. Assuming a uniform distribution of starting points for Brownian motion in Ω, the asymptotic and numerical results for the dimensional average second moment are given by

$$M_{\rm asy} \equiv \chi_{0H}/D_{\rm dim}^2\,, \qquad M_{\rm num} \equiv \frac{1}{|\Omega\setminus\Omega_p|}\int_{\Omega\setminus\Omega_p} M(\mathbf{x})\,d\mathbf{x}\,, \tag{6.16}$$

where $M = w/D_{\text{dim}}^2$ and χ_{0H} is obtained from the numerical solution of (6.13b) of Principal Result 6.1. In (6.16), Ω_p is the union of all the prey patches. Finally, we can then use the SMFPT and the MFPT to estimate the variance (VMFPT) of the first passage time. This variance is calculated using VMFPT = SMFPT − MFPT^2.

We first determine the effect of the location of a single circular patch within Ω on the SMFPT and VMFPT. In Fig. 15 we show a rather close agreement between the asymptotic and full numerical results for the average SMFPT (left panel) and the average VMFPT (right panel) as the distance r_0 of the center of the patch varies on $0 < r_0 < 1$. This figure shows that the average VMFPT increases rather significantly with the distance of the patch from the center of the disk. We can interpret this result in practical terms by comparing the standard deviation (square root of the VMFPT) to the MFPT, in both cases averaged over all possible starting positions. The MFPT corresponding to the results of Fig. 15 is plotted in Fig. 2. From these two figures, we can immediately see that for all locations of the single trap, the average standard deviation is close to the average MFPT. This means that the magnitude of the spread of likely values of the first passage time is comparable to the MFPT itself, at least when averaging over all possible starting positions. For this reason, the averaged MFPT is not a good estimator of actual search times in this scenario and caution should be employed when drawing biological conclusions based on this statistic alone.

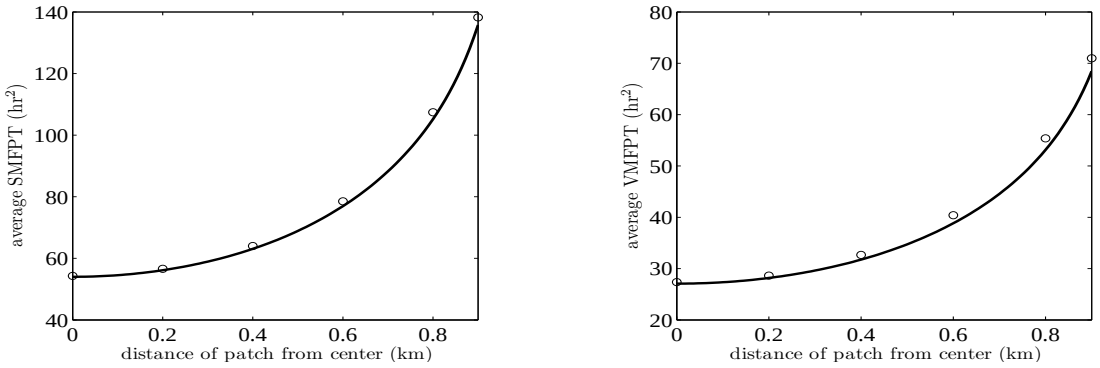

Fig. 15 Left panel: Plot of the average asymptotic SMFPT (solid curve) and the corresponding full numerical result (open circles) for one circular patch of radius $\varepsilon = 0.0067$ at a distance r_0 from the origin in the unit disk. Right panel: the asymptotic (solid curve) and the full numerical result (open circle) for the average VMFPT.

Next, we compare the numerical and asymptotic results for the average SMFPT and the average VMFPT when Ω contains three circular patches. The results for the SMFPT and VMFPT are shown in Table 9 for two configurations of three patches. For both patch arrangements in Ω, the asymptotic results for the SMFPT and the VMFPT obtained from Principal Result 6.1 are seen to compare reasonably favorably with the full numerical results computed from (6.15).

Patch1	Patch2	Patch3	SMFPT (asy)	SMFPT (num)	VMFPT (asy)	VMFPT (num)
(0.5,0.3)	(-0.2,0.6)	(-0.4,-0.7)	5.7593	5.8870	2.9095	3.0371
(0.3,0.8)	(0.1,-0.6)	(-0.5,-0.7)	8.0728	8.3361	4.0982	4.3621

Table 9 Spatial averages of the SMFPT and the VMFPT, measured in hr^2, for three circular patches of radius $\varepsilon = 0.0067$ in the unit disk. The asymptotic result is obtained from Principal Result 6.1 and the numerical results are computed from (6.15).

We remark that in contrast to the very close agreement between full numerics and asymptotics for the MFPT, the asymptotic and numerical results for the SMFPT and VMFPT in Table 9 do not agree as closely at the same ε. This is likely due to the fact that in asymptotically calculating the SMFPT from (6.2), we cannot use an exact solution for T in the Poisson equation, but instead we use its asymptotic approximation in the outer region. Without giving a formal error estimate, this does suggest that the asymptotic approximation of the SMFPT will not be as good as for the MFPT.

For our final example, we revisit the four-patch configuration of Fig. 9 with $D = 1$. Four circular patches of a common radius $\varepsilon = 0.025$ are equally-spaced on a ring of radius r_0 inside the unit disk. In the left panel of Fig. 16 we plot the asymptotic result for the average MFPT and the average VMFPT as a function of r_0, which assumes a uniformly distributed set of starting points for Brownian motion in the unit disk. As one might intuitively expect, these averaged quantities are smallest when (roughly speaking) the patches separate the unit disk into two halves of equal area. In the

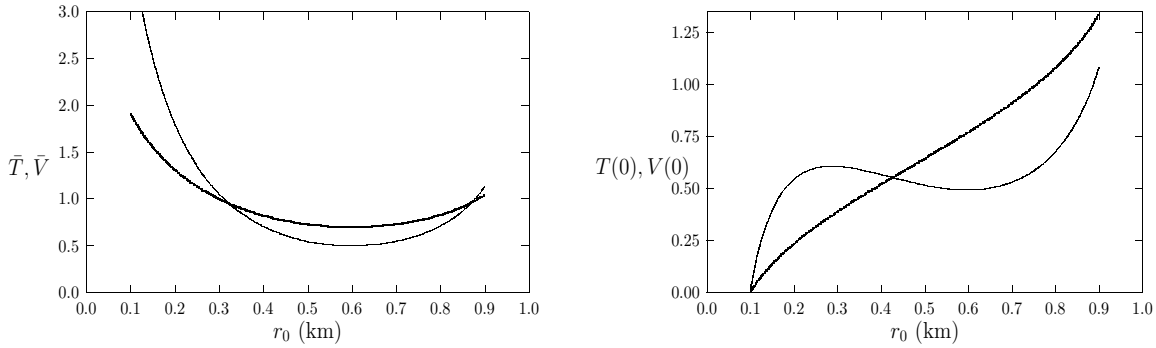

Fig. 16 Four circular patches of a common radius $\varepsilon = 0.025$ are equally-spaced on a ring of radius r_0 inside the unit disk (see the caption of Fig. 9). Left panel: plot of the dimensional asymptotic results for the average MFPT, $\bar{T}$(hr), heavy line, and the average VMFPT, $\bar{V}(\text{hr})^2$, as a function of r_0. Right panel: plot of the asymptotic results for the MFPT, $T(0)$(hr), heavy line, and the variance of the MFPT, $V(0)(\text{hr})^2$, versus r_0, for Brownian paths starting at the origin. The interpretation of these plots is given in the text.

right panel of Fig. 16 we plot asymptotic results for the MFPT and VMFPT for paths starting at the center of the disk. As expected, the MFPT increases monotonically with the distance r_0 of the patches from the origin. The non-monotone behavior of the VMFPT in the right panel of Fig. 16 can be interpreted as follows: For r_0 very small, the VMFPT is small since the predator is highly likely to quickly capture the prey when starting nearby at the origin. However, when r_0 is only moderately small, the predator is somewhat less likely to quickly capture the prey, and if the predator misses hitting a target site at first, it is likely to spend a large time wandering over a large territory without prey before returning to the region near the origin where the prey is located. This explains the local maximum of the VMFPT for moderately small r_0. For intermediate values of r_0, the VMFPT has a local minimum, as expected, when the ring of patches divide the unit disk into (roughly) two equal halves. The VMFPT increases again for larger r_0 since the predator will often wander over the large central territory before reaching any of the target sites near the boundary. We again notice that the standard deviation of the FPT is of similar magnitude to the MFPT and therefore the distribution of FPT is not well described by the MFPT alone.

7 Discussion

We have formulated and implemented semi-analytical methods to calculate the MFPT, the VMFPT, and the splitting probability, characterizing the movement of a predator searching for prey on a landscape with localized prey patches. The motion of the predator was assumed to have both a random and directed component. Our semi-analytical method exploits the assumption that the ratio of the radius of a typical prey patch to the overall length-scale of the landscape is asymptotically small. Results obtained from our asymptotic theory for the MFPT, the VMFPT, and the splitting probability were found to agree very favorably with corresponding full numerical results computed from the PDE's.

There are several further directions that could warrant investigation. First, we have only considered the case where the drift velocity in (2.1) can be written as the gradient of a scalar potential. Although the inner problems near the prey patches remain the same, for arbitrary drift velocities where (2.1) cannot be written in divergence form, it becomes somewhat more challenging to analyze the outer problem away from the small patches. Second, we have only considered Brownian motion with isotropic diffusivity. However, the motion of animals in the environment is likely more complicated than this. For example, it is known that wolves *(Canis Lupus)* tend to move rapidly along human-generated cuts in the forest environment (seismic lines related to oil and gas exploration) and this can potentially increase the encounter rate with prey [17, 26, 27, 36, 57, 58]. As shown in [35, 36], one way to model the behavior of a predator on a spatially heterogeneous landscape with a network of seismic lines is to replace the isotropic diffusion term $D\Delta' T$ in (2.1) with an anisotropic term of the form $D_{11}T_{xx} + D_{12}T_{xy} + D_{22}T_{yy}$ for some spatially varying positive coefficients D_{11}, D_{12}, and D_{22} determined by the specific seismic network topology. In principle, the hybrid asymptotic-numerical method developed in this paper can still be applied to this extended model to analytically extract the effect of small-scale prey patches, which are difficult to resolve numerically. Near the prey patches, where the diffusion coefficients are locally constant, one can formulate, after diagonalization of the diffusion operator, an inner problem similar to (2.6). However, the main new challenge in implementing a semi-analytical method for the MFPT would be to formulate, analyze, and then numerically

compute an appropriate Green's function that plays a key role in characterizing the outer solution away from the prey patches. Third, in our analysis we have assumed that the prey patches are stationary in time. The determination of the MFPT for the case of moving traps is a challenging open problem. Even for the simple case of one trap moving on a circular ring inside a disk, the MFPT was shown recently in [51] to exhibit qualitatively new behavior depending on the trap speed. As a fourth point, we have seen by calculating the VMFPT in a few experimental geometries that the full distribution of FPT might not be well described by its mean alone. This indicates that the MFPT may actually be quite an imprecise tool when applied in ecological modelling. We intend to take up this question in future work.

Finally, our analysis has focused only on deriving averaged quantities for predator motion such as the MFPT and VMFPT. These quantities arise naturally in the long-time approximation of the probability density function $p(\mathbf{x},t)$ of finding the predator at position $\mathbf{x}\in\Omega$ at time t. With the goal of including short-time information for the first passage density, in [23] uniform in time approximations for $p(\mathbf{x},t)$ were derived for a 3-D domain containing a small spherical target. It would be interesting to extend the analysis of [23] to our 2-D context.

Acknowledgements

V. K. acknowledges support from the Pacific Institute for Mathematical Sciences International Graduate Training Center in Mathematical Biology. J. C. T. was supported by an AARMS (Atlantic Canada) Postdoctoral Fellowship. D. C. and M. J. W. gratefully acknowledge grant support from NSERC (Canada). We are grateful to an anonymous referee for helping clarify the result in Fig. 9.

A The Logarithmic Capacitance of a Two-Disk Cluster

We first derive the result (5.15) for the logarithmic capacitance d_{1c} of two disjoint circular patches $\Omega_{1,0}$ and $\Omega_{1,1}$ of radii a_0 and a_1, respectively. Since d_{1c} is invariant under coordinate rotations, we can without loss of generality choose the centers of the circles to lie along the horizontal $y_2=0$ axis at some $y_1=b_0>0$ and $y_1=-b_1<0$, respectively.

For this special two-trap cluster, the inner problem (5.14) with $\mathbf{y}=(y_1,y_2)$, is

$$\begin{aligned}&\Delta_{\mathbf{y}} q_c=0\,,\quad \mathbf{y}\notin\Omega_{1,j}\,,\quad j=0,1\,;\qquad q=0\,,\quad \mathbf{y}\in\partial\Omega_{1,j}\,,\quad j=0,1\,,\\ &\qquad q\sim\log|\mathbf{y}|\,,\quad \text{as}\quad |\mathbf{y}|=(y_1^2+y_2^2)^{1/2}\to\infty\,,\end{aligned}\tag{A.1}$$

where $\Omega_{1,1}$ and $\Omega_{1,0}$ are the circles $(y_1+b_1)^2+y_2^2=a_1^2$ and $(y_1-b_0)^2+y_2^2=a_0^2$, respectively. The logarithmic capacitance d_{1c} of the two-circle cluster is defined in terms of the solution to (A.1) by the far-field condition

$$q_c-\log|\mathbf{y}|=-\log d+o(1)\,,\quad \text{as}\quad |\mathbf{y}|=(y_1^2+y_2^2)^{1/2}\to\infty\,.\tag{A.2}$$

To solve (A.1) we introduce bipolar coordinates ξ and η defined by

$$y_1=\frac{c\sinh\xi}{\cosh\xi-\cos\eta}\,,\qquad y_2=\frac{c\sin\eta}{\cosh\xi-\cos\eta}\,.\tag{A.3}$$

Then, $|\mathbf{y}|\to\infty$ corresponds to $\rho\equiv(\xi^2+\eta^2)^{1/2}\to 0$. From (A.3) we obtain $|\mathbf{y}|\sim 2c/\rho$ as $|\mathbf{y}|\to\infty$. Therefore, the far-field behavior in (A.1) is equivalent to $q_c\sim-\log\rho$ as $\rho=(\xi^2+\eta^2)^{1/2}\to 0$.

With bipolar coordinates, lines of constant ξ map to disks of the form $(y_1-y_c)^2+y_2^2=a^2$, where $y_c=c/\tanh\xi$ and $a=c/|\sinh\xi|$. As such, the right circle $\Omega_{1,0}$ with center $\mathbf{y}=(b_0,0)$ and radius a_0, corresponds to $\xi=\xi_0>0$, where

$$a_0=c/\sinh\xi_0\,,\qquad b_0=c/\tanh\xi_0\,.\tag{A.4}$$

In contrast, the left circle $\Omega_{1,1}$ with center $\mathbf{y}=(-b_1,0)$ and radius a_1, corresponds to $\xi=-\xi_1<0$, so that $\xi_1>0$, where

$$a_1=c/\sinh\xi_1\,,\qquad b_1=c/\tanh\xi_1\,.\tag{A.5}$$

We label the center-to-center distance between the two disks as l, so that $l=b_0+b_1$.

From (A.4) and (A.5), we obtain that $\xi_0>0$, $\xi_1>0$ and c are determined in terms of the disk radii a_0 and a_1, and the center-to-center distance l, by the three equations

$$a_0=c/\sinh\xi_0\,,\qquad a_1=c/\sinh\xi_1\,,\qquad l=c/\tanh\xi_0+c/\tanh\xi_1\,.\tag{A.6}$$

From this system, we readily derive that $l=\sqrt{c^2+a_0^2}+\sqrt{c^2+a_1^2}$. By squaring this relation, we can solve for c in terms of l to obtain, after some algebra, that c is given by (5.16). With c known, ξ_0 and ξ_1 are obtained as in (5.17). We remark, that with c as given in (5.16), the centers of the two disks are at $\mathbf{y}=(\sqrt{c^2+a_0^2},0)$ and $\mathbf{y}=(-\sqrt{c^2+a_1^2},0)$.

Upon transforming (A.1) to bipolar coordinates, we obtain that $Q(\xi,\eta) \equiv q_c\left[y_1(\xi,\eta), y_2(\xi,\eta)\right]$ satisfies

$$\begin{gathered} Q_{\xi\xi} + Q_{\eta\eta} = 0\,, \quad -\xi_1 \le \xi \le \xi_0\,, \quad |\eta| \le \pi\,, \\ Q = 0 \quad \text{on} \quad \xi = -\xi_1\,,\ \ \xi = \xi_0\,; \qquad Q\,, Q_\eta \quad 2\pi \text{ periodic in } \eta\,, \\ Q \sim -\frac{1}{2}\log\left(\xi^2+\eta^2\right) + \mathcal{O}(1)\,, \quad \text{as} \quad \xi^2+\eta^2 \to 0\,. \end{gathered} \tag{A.7}$$

To solve (A.7), we first observe that a special solution to $Q_{\xi\xi} + Q_{\eta\eta} = 0$ with the singularity behavior in (A.7) is

$$Q_f(\xi,\eta) \equiv -\frac{1}{2}\log\left(\cosh\xi - \cos\eta\right) = -\frac{|\xi|}{2} + \frac{\log 2}{2} + \sum_{m=1}^{\infty}\frac{e^{-m|\xi|}}{m}\cos(m\eta)\,. \tag{A.8}$$

We then decompose $Q = Q_f + Q_p$, so that Q_p satisfies $\Delta_{\mathbf{y}} Q_p = 0$, is 2π periodic in η, and satisfies the boundary conditions

$$Q_p(\xi_0,\eta) = \frac{\xi_0}{2} - \frac{\log 2}{2} - \sum_{m=1}^{\infty}\frac{e^{-m\xi_0}}{m}\cos(m\eta)\,, \qquad Q_p(-\xi_1,\eta) = \frac{\xi_1}{2} - \frac{\log 2}{2} - \sum_{m=1}^{\infty}\frac{e^{-m\xi_1}}{m}\cos(m\eta)\,. \tag{A.9}$$

To determine Q_p, we first represent Q_p as a Fourier cosine series in $\cos(m\eta)$ and then use the boundary conditions (A.9) to identify the coefficients in the Fourier series. In this way, we obtain that

$$Q_p(\xi,\eta) = C_0 + D_0\xi + \sum_{m=1}^{\infty}\left[C_m\cosh(m\xi) + D_m\sinh(m\xi)\right]\cos(m\eta)\,, \tag{A.10a}$$

where

$$C_0 = -\frac{\log 2}{2} + \frac{\xi_0\xi_1}{\xi_0+\xi_1}\,; \qquad C_m = -\frac{\left[e^{-m\xi_0}\sinh(m\xi_1) + e^{-m\xi_1}\sinh(m\xi_0)\right]}{m\sinh\left[m(\xi_0+\xi_1)\right]}\,, \quad \text{for} \quad m \ge 1\,, \tag{A.10b}$$

with similar formulae for the coefficients D_m for $m \ge 0$.

Finally, to identify the logarithmic capacitance d_{1c} of the cluster, we expand $Q = Q_f + Q_p$ as $(\xi,\eta) \to 0$ to obtain

$$Q \sim -\frac{1}{2}\log\left(\frac{\xi^2+\eta^2}{2}\right) + Q_p(0,0)\,. \tag{A.11}$$

Since $\xi^2+\eta^2 \sim 4c^2/|\mathbf{y}|^2$ from (A.3), we obtain from (A.11) that

$$q_c \sim \log|\mathbf{y}| - \log\left(2\sqrt{c}\right) + Q_p(0,0)\,, \quad \text{as} \quad |\mathbf{y}| \to \infty\,. \tag{A.12}$$

From this relation, together with $Q_p(0,0) = \sum_{m=0}^{\infty} C_m$ from (A.10), we identify d_{1c} in (A.2) as

$$\log d_{1c} = \log(2c) - \frac{\xi_0\xi_1}{\xi_0+\xi_1} - \sum_{m=1}^{\infty} C_m\,, \tag{A.13}$$

where C_m for $m \ge 1$ is given in (A.10b). This completes the derivation of (5.15).

Next, we derive (5.18) for $q_\infty^\star$ by first transforming (5.13) to bipolar coordinates. In this way, we obtain that $Q^\star(\xi,\eta) \equiv q^\star\left[y_1(\xi,\eta), y_2(\xi,\eta)\right]$ is the smooth function that satisfies

$$\begin{gathered} Q^\star_{\xi\xi} + Q^\star_{\eta\eta} = 0\,, \quad -\xi_1 \le \xi \le \xi_0\,, \quad |\eta| \le \pi\,, \\ Q^\star = 0 \quad \text{on} \quad \xi = -\xi_1\,; \qquad Q^\star = 1 \quad \text{on} \quad \xi = \xi_0\,; \qquad Q^\star\,, Q^\star_\eta \quad 2\pi \text{ periodic in } \eta\,. \end{gathered} \tag{A.14}$$

The solution to this problem is simply $Q^\star = (\xi+\xi_1)/(\xi_0+\xi_1)$. Since $r \to \infty$ as $(\xi,\eta) \to 0$, we readily identify the far-field behavior in (5.13) as $q_\infty^\star = Q^\star(0,0) = \xi_1/(\xi_0+\xi_1)$, which confirms (5.18).

References

1. C. Amoruso, T. Lagache, D. Holcman, *Modeling the early steps of cytoplasmic trafficking in viral infection and gene delivery*, SIAM J. Appl. Math., **71**(6), (2011), pp. 2334–2358.
2. F. Bartumeus, M. G. E. Da Luz, G. M. Viswanathan, J. Catalan, *Animal search strategies: a quantitative random-walk analysis*, Ecology, **86**(11), (2005), pp. 3078–3087.
3. O. Benichou, R. Voituriez, *From first-passage times of random walks in confinement to geometry-controlled kinetics*, Physics Reports, **539**, (2014), pp. 225–284.
4. H. C. Berg, *Random walks in biology*, Princeton University Press, Princeton, New Jersey, 1983.
5. P. C. Bressloff, B. A. Earnshaw, M. J. Ward, *Diffusion of protein receptors on a cylindrical dendritic membrane with partially absorbing traps*, SIAM J. Appl. Math., **68**(5), (2008), pp. 1223–1246.
6. P. C. Bressloff, J. Newby, *Stochastic models of intracellular transport*, Rev. Mod. Physics, **85**, (2013), pp. 135–196.

7. C. Caginalp, X. Chen, *Analytical and numerical results for an escape problem*, Arch. Rational Mech. Anal., **203**, (2012), pp. 329–342.
8. X. Chen, A. Friedman, *Asymptotic analysis for the narrow escape problem*, SIAM J. Math. Anal., **43**, (2011), pp. 2542–2563.
9. C. Chevalier, O. Benichou, B. Meyer, R. Voituriez, *First passage quantities of brownian motion in a bounded domain with multiple targets: a unified approach*, J. Phys A: Math. Theor., **44**, (2011), 025002 (24 pp).
10. A. Cheviakov, M. J. Ward, *Optimizing the fundamental eigenvalue of the laplacian in a sphere with interior traps*, Math. Comp. Modeling, **53**, (2011), pp. 1394–1409.
11. C. A. Cobbold, F. Lutscher, *Mean occupancy time: linking mechanistic movement models, population dynamics and landscape ecology to population persistence*, J. Math. Biol., **68**(3), (2014), pp. 549–579.
12. S. Condamin, O. Benichou, M. Moreau, *Random walks and brownian motion: a method of computation of first-passage times and related quantities in confined geometries*, Phys. Rev. E., **75**, (2007), 021111 (20 pp).
13. D. Coombs, R. Straube, M. J. Ward, *Diffusion on a sphere with localized traps: mean first passage time, eigenvalue asymptotics, and fekete points*, SIAM J. Appl. Math., **70**(1), (2009), pp. 302–332.
14. W. Dijkstra, M. E. Hochstenbach, *Numerical approximation of the logarithmic capacity*, CASA Report 08-09, Technical U. Eindhoven, preprint, (2008).
15. O. Dushek, D. Coombs, *Analysis of serial engagement and peptide-MHC transport in T cell receptor microclusters*, Biophys. J., **94**(9), (2008), pp. 3447–3460.
16. FlexPDE6, *PDE Solutions Inc.*, URL http://www.pdesolutions.com
17. J. Frair, E. Merrill, D. Visscher, D. Fortin, H. Beyer, J. Morales, *Scales of movement by elk (Cervus elaphus) in response to heterogeneity in forage resources and predation risk*, Landscape Ecol. **20**(3) (2005), pp. 273–287.
18. C. Gardiner, *Stochastic methods, a handbook for the natural and social sciences (4th edition)*, Springer-Verlag, Berlin, 2009.
19. E. Gurarie, O. Ovaskainen, *characteristic spatial and temporal scales unify models of animal movement*, American Naturalist, **178**(1), (2011), pp. 113–123.
20. E. Gurarie, O. Ovaskainen, *towards a general formalization of encounter rates in ecology*, Theor. Ecology, **6**(2), (2013), pp. 189–202.
21. D. Holcman, Z. Schuss, *The narrow escape problem*, SIAM Review, **56**(2), (2014), pp. 213–257.
22. P Holgate, *Random walk models for animal behavior*, in G. Patil, E. Pielou, W. Waters, editors, *Statistical Ecology*, Volume 2, pp. 1–12. Penn. State Univ. Press, 1971.
23. S. Isaacson, J. Newby, *Uniform asymptotic approximation of diffusion to a small target*, Phys. Rev. E., **88** 012820 (2013) (13 pp).
24. A. James, M. J. Plank, R. Brown, *Optimizing the encounter rate in biological interactions: ballistic versus lévy versus brownian strategies*, Phys. Rev. E. Stat. Nonlin. Soft Matter Phys., **78**(1), (2008), 051128. 2008.
25. A. James, J. W. Pitchford, M. J. Plank, *Efficient or inaccurate? analytical and numerical modelling of random search strategies*, Bull. Math. Biology, **72**(4), (2010), pp. 896–913.
26. A. James, *Effects of industrial development on the predator-prey relationship between wolves and caribou in Northeastern Alberta*, Ph. D thesis, University of Alberta, (1999).
27. A. James, A. Stuart-Smith, *Distribution of caribou and wolves in relation to linear corridors*, J. Wildl. Manag., **64**(1), (2000) pp. 154–159.
28. P. Kareiva, A. Mullen, R. Southwood, *Population dynamics in spatially complex environments: theory and data and discussion*, Phil. Trans.: Biol. Sci. **330**, (1990), pp. 175–190.
29. J. Kevorkian, J. Cole, *Multiple scale and singular perturbation methods*, Applied Mathematical Sciences, Vol. 114, Springer-Verlag, New York, 1996.
30. T. Kolokolnikov, M. Titcombe, M. J. Ward, *Optimizing the fundamental neumann eigenvalue for the laplacian in a domain with small traps*, European J. Appl. Math., **16**(2), (2005), pp. 161–200.
31. T. Lagache, E. Dauty, D. Holcman, *Quantitative analysis of virus and plasmid trafficking in cells*, Phys Rev. E., **79**, 011921, (2009).
32. T. Lagache, D. Holcman, *Effective motion of a virus trafficking inside a biological cell*, SIAM J. Appl. Math., **68**(4), (2008), pp. 1146–1167.
33. T. Lagache, D. Holcman, *Quantifying the intermittent transport in the cell cytoplasm*, Phys. Rev. E., **77**, 030901(R), (2008).
34. S.L. Lima, P.A. Zollner, *Towards a behavioral ecology of ecological landscapes*, Trends Ecol. Evol., **11**(3), (1996), pp. 131–135.
35. H. McKenzie, M. Lewis, E. Merrill, *First passage time analysis of animal movement and insights into the functional response*, Bull. Math. Biology, **71**, (2009), pp. 107–129.
36. H. McKenzie, E. Merrill, R. Spiteri, M. Lewis, *How linear features alter predator movement and the functional response*, Interface Focus, **2**, (2012), pp. 205–216.
37. P. Moorcroft, M.A. Lewis, *Mechanistic home range analysis*, (2006), Princeton University Press, Princeton, NJ.
38. A. Okubo, S. Levin, *Diffusion and ecological problems*, Springer-Verlag, Berlin, 1991.
39. S. Pillay, M. J. Ward, A. Peirce, T. Kolokolnikov, *An asymptotic analysis of the mean first passage time for narrow escape problems: Part I: two-dimensional domains*, SIAM J. Multiscale Modeling and Simulation, **8**(3), (2010), pp. 803–835.
40. T. Ransford, *Potential theory in the complex plane*, London Math. Soc. Stud. Texts 28, Cambridge Univ. Press, (1995), Cambridge, U.K.
41. S. Redner, *A guide to first-passage time processes*, Cambridge Univ. Press, Cambridge, U.K., 2001
42. A. Singer, Z. Schuss, *Activation through a narrow opening*, SIAM J. Appl. Math., **68**(1), (2007), pp. 98–108.
43. A. Singer, Z. Schuss, D. Holcman, *Narrow escape, part ii: the circular disk*, **122**(3), J. Stat. Physics, (2006), pp. 465–489.
44. Z. Schuss, *The narrow escape problem - a short review of recent results*, J. Sci. Computing, **53**(1), (2012), pp. 194–210.
45. Z. Schuss, *Theory and applications of stochastic processes; an analytical approach*, Springer, Applied Mathematical Sciences, Vol. 170, (2010).
46. J. Skellam, *Random dispersal in theoretical populations*, Biometrika, **38**, (1951), pp. 196-218.
47. R. Straube, M. J. Ward, M. Falcke, *Reaction-rate of small diffusing molecules on a cylindrical membrane*, J. Stat. Physics, **129**(2), (2007), pp. 377–405.
48. A. H. Stroud, *Approximate calculation of multiple integrals*, Prentice-Hall, Englewood Cliffs, New Jersey, (1971).

49. A. Taflia, D. Holcman, *Dwell time of a brownian molecule in a microdomain with traps and a small hole on the boundary*, J. Chem. Physics, **126**, 234107, (2007), (12 pp).
50. K. Tsaneva, A. Burgo, T. Galli, D. Holcman, *Modeling neurite growth*, Biophysical J., **96**(3), (2009), pp. 840-857.
51. J. Tzou, T. Kolokonikov, *Mean first passage time for a small rotating trap inside a reflective disk*, to appear, SIAM J. Multiscale Modeling and Simulation, (2015).
52. M. Titcombe, M. J. Ward, *An asymptotic study of oxygen transport from multiple capillaries to skeletal muscle tissue*, SIAM J. Appl. Math., **60**(5), (2000), pp. 1767–1788.
53. P. Turchin, *Translanting foraging movements in heterogeneous environments into the spatial distribution of foragers*, Ecology **72**(4), (1991), pp. 1253–1266.
54. P. Turchin, *Quantitative analysis of movement: measuring and modeling population redistribution in animals and plants*, (1998), Sinauer Associates, Sunderland, MA.
55. M. J. Ward, W. D. Henshaw, J. Keller, *Summing logarithmic expansions for singularly perturbed eigenvalue problems*, SIAM J. Appl. Math., **53**(3), (1993), pp. 799–828.
56. M. J. Ward, J. B. Keller, *Strong localized perturbations of eigenvalue problems*, SIAM J. Appl. Math., **53**(3), (1993), pp. 770–798.
57. J. Whittington, C.C. St Clair, G. Mercer, *Path tortuosity and the permeability of roads and trails to wolf movement*, Ecol. Soc., **9**(1), 4 (2004).
58. J. Whittington, C.C. St Clair, G. Mercer, *Spatial responses of wolves to roads and trails in mountain valleys*, Ecol. Appl., **15**, (2005), pp. 543 – 553.